Energy Conversion and Management 345 (2025) 120251

Contents lists available at ScienceDirect

Energy Conversion and Management

journal homepage: www.elsevier.com/locate/enconman

Research paper

Optimal control strategy for the operation of a PEMFC system under low-pressure conditions

Dominik Murschenhofer *, Jonas Settele, Cornelie Bänsch

German Aerospace Center (DLR), Institute of Engineering Thermodynamics, Pfaffenwaldring 38–40, 70569, Stuttgart, Germany

ARTICLE INFO

Keywords:
PEMFC
Fuel cell system
Low-pressure operation
Design of experiment
Performance optimization
Control strategy

ABSTRACT

The effect of low ambient pressure on a PEMFC system is investigated by operating the entire non-pressurized fuel cell system inside a low-pressure chamber. Polarization curve measurements are conducted at various pressure levels between 980 and 491 hPa by using the manufacturer's default parameters for stack temperature and cathode stoichiometry control. Significant net power losses of up to 59 % at 491 hPa are observed with respect to 980 hPa, which result from increasing stack drying and growing parasitic power losses with decreasing pressure. The latter is due to the decreasing fluid density combined with a constant mass flow requirement. Using statistical design of experiment methods, a comprehensive parameter study is performed to derive model equations for the response of the cell voltage, the net power and the relative humidity at low-pressure operation. The model predictions are in very good agreement with validation measurements. Model evaluation yields the pressure and current density-dependent optimal parameters for stack temperature and cathode stoichiometry control in terms of the net power output. Applying the optimal control parameters to the experiment leads to significantly higher cell efficiency and net power compared to the use of the default parameters. At 497 hPa, a net power increase of 29 % is observed experimentally. The model analysis shows that, in good approximation, the optimal relative humidity is independent of the pressure and decreases linearly with rising current density. Moreover, the optimal stack temperature is, in a first approximation, independent of the current density and decreases linearly with decreasing pressure. Based on these two linear relations, a simplified optimal operation strategy is proposed to obtain high net power output at low ambient pressure.

1. Introduction

The use of polymer electrolyte membrane fuel cells (PEMFCs) as power source is a promising approach to contribute to the decarbonization of the aviation sector [1–5]. However, the low ambient pressure associated to high-altitude conditions presents a fundamental challenge for the operation of PEMFC systems in aviation and other high-altitude applications [6]. At reduced pressures, PEMFC systems suffer from significant performance losses, primarily due to lowered oxygen partial pressure [7], deteriorating membrane hydration [8], and increased parasitic losses [9]. These effects lead to substantial reductions in net power output and overall system efficiency [10–17], thereby limiting the viability of fuel cells in real-world aviation applications.

Addressing these challenges requires a precise understanding of how operating parameters such as stack temperature, cathode stoichiometry, and stack humidification interact under low-pressure conditions and affect the fuel cell's performance. Previous studies have provided important insights into this issue. Chang and Gallman [15] and Spiegel et al. [16] reported net power drops of 25 % and 24 % at moderate altitudes of 1524 m and 2256 m, respectively. According to the ICAO standard atmosphere [18], the altitudes reported by [15,16] correspond to operating pressures of 843 hPa and 770 hPa, respectively. Graf et al. [17] presented dynamically observed current–voltage curves at different low-pressure levels of a 100 cells Hydrogenics HD10 type fuel cell stack, i.e. the same fuel cell type as the unit under test in the present paper. Compared to the maximum gross power output at 900 hPa, a power loss of 46 % can be observed from their measurements at an ambient pressure of 300 hPa.

Hordé et al. [19] experimentally investigated the effect of cathode stoichiometry variation on a PEMFC at low operating pressures. Applying a stoichiometry of 2, the power output at 780 hPa dropped by 48 % with respect to 1001 hPa. However, the power drop could be reduced to only 5 % by increasing the stoichiometry to 2.5, which indicates a large optimization potential due to parameter optimization. Werner et al. [20,21] performed stack temperature variations combined with moderate stoichiometry variations at low operating pressures (950 – 700 hPa). With regard to stack gross power, they concluded that

* Corresponding author.
E-mail address: dominik.murschenhofer@dlr.de (D. Murschenhofer).

https://doi.org/10.1016/j.enconman.2025.120251
Received 30 March 2025; Received in revised form 4 July 2025; Accepted 17 July 2025
Available online 13 August 2025

Nomenclature

Latin letters

i	Current density, A/cm^2
p	Chamber pressure, hPa
P_{net}	Net power, W
p_{out}	Pressure at the cathode outlet, hPa
$p_{sat}(T_{out})$	Saturation vapor pressure as function of the cathode outlet temperature, hPa
rH	Relative humidity, %
r_{O2}	Oxygen concentration at the cathode inlet, –
T	Stack temperature, °C
t	Runtime, h
U	Average cell voltage, V

Greek letters

η	Cell efficiency based on the LHV of hydrogen, %
λ	Cathode stoichiometry, –

Abbreviations

ANOVA	Analysis of variance
ATLAS	Altitude test chamber for low-pressure analysis of fuel cell systems
BoP	Balance of plant
C.V.	Coefficient of variation
df	Degree of freedom
DoE	Design of experiment
ICAO	International Civil Aviation Organization
LHV	Lower heating value
PEMFC	Polymer electrolyte membrane fuel cell
PRESS	Predicted residual sum of squares
RMSE	Root mean square error

stoichiometry variations play a subordinate role compared to stack temperature adaption.

Pessot et al. [22] characterized the performance of a 1 kW PEMFC at varying inlet gas pressure (1500 – 800 hPa), fuel cell temperature and inlet relative humidity of air and hydrogen, based on data obtained with design of experiment methods. They derived a polarization curve model as a function of the operating parameters and showed reasonable prediction capability of the model by using parameters that lie outside the model's validity limits, i.e. at gas pressures of 1700 hPa and 650 hPa.

In the named previous studies, PEMFCs were primarily characterized at discrete low-pressure levels and some indications how to overcome the associated power losses were given. What remains missing is a comprehensive, pressure-dependent control strategy that integrates all critical parameters into a unified framework maximizing net power across a wide range of ambient pressures [23].

Many altitude control approaches mainly focus on the optimization of the air supply system [24–28]. While pressurization effectively leads to higher fuel cell power output, the membrane humidification strongly depends on both cathode stoichiometry and stack temperature. The latter has been widely neglected in previously presented altitude control strategies.

The present paper addresses that gap and presents pressure- and current-density-dependent control functions for cathode stoichiometry and stack temperature that are continuous and readily applicable in real-time control systems, enabling dynamic adaptation in variable-pressure environments such as flight. To this end, a comprehensive parameter study is performed to identify the optimal operating conditions of a PEMFC system with regard to aviation application. Based on the results, the control functions are derived by utilizing a design of experiment approach. Eventually, the presented novel optimization method will be transferable to various other fuel cell systems to maintain high performance under strongly changing ambient pressure.

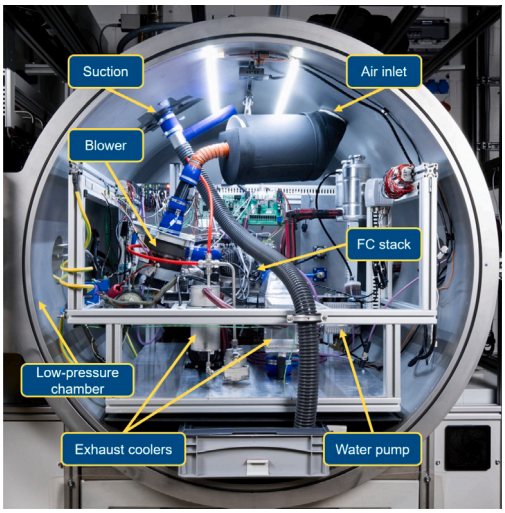

Fig. 1. ATLAS testbed setup with open door of the low-pressure chamber.

In Section 2 the testbed setup including the fuel cell system configuration is described in detail. In Section 3 the testing and evaluation procedures as well as the design of experiment approach are presented. In Section 4 the experimental and modeling results are discussed and validated. Moreover, an optimal control strategy for low-pressure operation is proposed. Finally, the conclusions of the study are presented in Section 5 and future research perspectives are suggested in Section 6.

2. Experimental setup

The low-pressure test environment, called ATLAS (Altitude Test chamber for Low-pressure Analysis of fuel cell Systems), consists of a low-pressure chamber to which a vacuum pump is connected. The chamber is supplied with dry compressed air through a mass flow controller and the pressure is controlled by a pressure regulator. Furthermore, it is possible to control the inlet air temperature by a process thermostat.

The fuel cell system is operated inside the low-pressure chamber and is composed of a self-humidifying 120 cells Hydrogenics HyPM HD 10-120 PEMFC stack [29] with an active cell area of 195 cm^2 and 12 kW nominal power output, an anode recirculation pump and a cooling unit. A blower supplies the cathode inlet with air from the low-pressure atmosphere. Due to a pressure coupling between anode and cathode, where the anode pressure is constantly kept about 40 hPa above the cathode pressure, both sides are affected by the low-pressure environment. Besides the primary cooling system of the stack, a secondary cooling circuit is installed for separating the product water from both anode and cathode exhaust gas. An insight into the ATLAS test environment is given in Fig. 1.

While the balance of plant (BoP) components are powered by an auxiliary power supply, the components' individual power demands are measured to determine the system's net power output. The fuel cell stack is equipped with a cell voltage monitoring board, which measures the mean voltages of 60 cell pairs. Inside the low-pressure chamber, the pressure, temperature, relative humidity, and hydrogen and oxygen concentrations of the test atmosphere are measured. Besides various pressure and temperature probes distributed across the anode and cathode systems, the relative humidity is measured at the cathode outlet. The latter is used as an indication of the stack humidification,

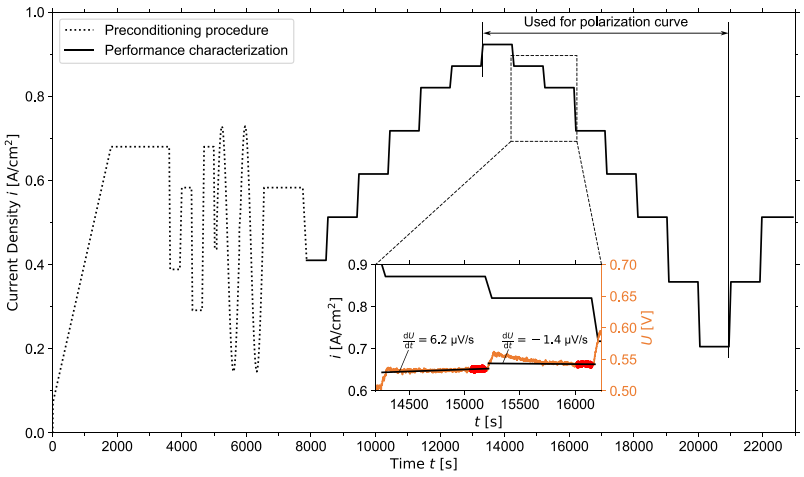

Fig. 2. Example of the preconditioning procedure and polarization curve measurement. The close-up shows the current density steps and the corresponding averaged cell voltage response U as orange line. The last 120 s of each step, indicated in red, are used to determine the steady-state mean value of U. The black lines in the close-up represent the regression line of the measured voltage response during the red 120 s averaging interval.

although complex internal humidification phenomena as well as liquid water formation are not represented by the sensor. To investigate these effects, either supporting numerical simulations [30,31] or single cell tests [32] would be required.

Hydrogen for the electrochemical reaction and nitrogen for the inertization of the fuel cell are provided by large in-house supply tanks. The electricity produced by the fuel cell is fed into the grid via an electrical load. The waste heat is discharged via the in-house cooling circuit.

The fuel cell system features a controller board, which controls the BoP components, i.e. the air blower, the hydrogen recirculation pump and the hydrogen supply and purge valves, according to the desired power demand. The communication with the FC controller board is implemented into a custom built LabView program, used to control the entire testbed.

Detailed piping and instrumentation diagrams of the inside and outside of the ATLAS low-pressure chamber are shown in Appendix A, Fig. A.13 and Fig. A.14, respectively. A list of the implemented sensors is given in Appendix A, Table A.6.

3. Methods and procedures

3.1. Testing procedures

Prior to all tests, a preconditioning procedure, i.e. an empirically defined load cycle shown as dotted line in Fig. 2, is applied in order to minimize the influence of reversible degradation and to set the fuel cell into a well defined and reproducible state. Preconditioning is repeated at the beginning of each testing day.

To investigate the effect of low ambient pressure on the performance of the fuel cell, polarization curves are measured at different pressure levels (1000−500 hPa) using the manufacturer's default parameters for stack temperature and cathode stoichiometry control, which solely depend on the current density i, see Table 1 and the dashed lines in Figs. 7a and b. The polarization curves are measured by stepwise increasing the current density to the maximum value such that the average cell voltage U is about 0.5 V. Then, the current density is stepwise decreased to a minimum value such that the average cell voltage is about 0.75 V, see the solid line in Fig. 2.

To identify the optimal operating conditions for low-pressure operation of the PEMFC system, a widespread parameter study is performed, where the stack temperature T and the cathode stoichiometry λ are varied at different current density i and chamber pressure p levels. The parameter study is performed the following way: After the preconditioning procedure at the beginning of each testing day, the system

Table 1
Default parameters for T and λ control of a Hydrogenics HyPM HD 10-120 PEMFC stack, depending solely on i.

i [A/cm²]	T [°C]	λ [–]
0.00	50.0	2.86
0.09	50.0	2.68
0.10	50.3	2.66
0.24	55.0	2.66
0.30	55.0	2.66
0.40	55.0	2.46
0.50	55.0	2.46
0.70	60.0	2.46
0.90	60.0	2.46

performance is measured at a reference point, i.e. p = 750 hPa, i = 0.51 A/cm², T = 55.0 °C and λ = 2.36, to keep track of the performance evolution during the test campaign. In the next step, the chamber pressure is set to the desired level and kept constant for the rest of the day. The steady-state measuring points are determined by choosing the stack temperature and cathode stoichiometry values according to the test plan, see Section 3.2. The measuring points of the parameter study are recorded with monotonically increasing current density to avoid hysteresis effects, cf. e.g. [7].

The experiments are carried out under defined conditions, where the oxygen concentration inside the test chamber is > 19.6 % and the temperature just in front of the air blower is kept constant at 20.0 °C. It is assumed, that a steady state is reached when the two following criteria are met: First, all control parameters have been held constant for at least 12 minutes to avoid the incorporation of dynamic effects due to the state change. Second, the rate of change of the average cell voltage $|dU/dt| < 10$ µV/s, which is determined by calculating the slope of the regression line of the measured average cell voltage during a 120 s interval used to determine the steady-state mean values, see the close-up in Fig. 2. Note that dynamic effects such as membrane hydration or dehydration are represented by a changing voltage response such that in some cases the second criterion leads to dwell times of more than 20 min, if the fuel cell is exposed to extreme conditions.

In Appendix A, Table A.6, all sensors implemented in the ATLAS testbed, which have been calibrated prior to the test campaign, are listed together with their measurement uncertainties. In all following figures showing experimental data, the associated measurement errors are visualized as error bars. Since not all measurement uncertainties can be considered as independent and random (e.g. the dependence of the relative humidity measurement on the temperature probe at

Table 2
Treatment factors and the corresponding levels of the parameter space investigated in course of the parameter study.

Factor	No. of levels	Levels
p [hPa]	6	500, 600, 700, 800, 900, 1000
i [A/cm^2]	20	0.13, 0.26, 0.33, 0.38, 0.44, 0.49, 0.51, 0.54, 0.59, 0.64, 0.67, 0.69, 0.74, 0.77, 0.79, 0.85, 0.87, 0.90, 0.92, 0.95
T [°C]	16	40.0, 42.0, 44.0, 46.0, 48.0, 50.0, 52.0, 54.0, 56.0, 58.0, 60.0, 62.0,64.0, 66.0, 68.0, 70.0
λ [–]	9	2.0, 2.2, 2.4, 2.6, 2.8, 3.0, 3.2, 3.4, 3.6

Table 3
Limiting values of the current density, the stack temperature and the cathode stoichiometry applied during the parameter study at each pressure level.

p [hPa]	i [A/cm^2]		T [°C]		λ [–]	
	min.	max.	min.	max.	min.	max.
1000	0.26	0.95	50.0	70.0	2.0	3.6
900	0.26	0.92	48.0	70.0	2.0	3.6
800	0.13	0.90	46.0	70.0	2.0	3.6
700	0.13	0.77	42.0	68.0	2.0	3.6
600	0.13	0.67	40.0	64.0	2.0	3.6
500	0.13	0.51	40.0	60.0	2.0	3.6

the corresponding position), a conservative error calculation is applied, [33]. Therefore, the error of a quantity calculated by a sum or difference is determined by the sum of the individual errors. The fractional error, i.e. the error divided by the measured value, of a quantity calculated by a multiplication or division is determined by the sum of the individual fractional errors.

3.2. Design of experiment

The investigation and optimization of complex systems often requires a large number of experiments, especially when multidimensional parameter spaces are analyzed. In such cases, statistical methods may be applied to analyze parameter interactions and to reduce the required number of experimental runs. A well-established approach is the statistical design of experiments (DoE), which allows to identify optimal parameter combinations, e.g. for maximum performance, and dependencies between different factors, [34,35].

DoE methods are widely used in a variety of scientific and engineering disciplines, including fuel cell research and development [21,22,36–41]. They allow efficient evaluation, modeling and optimization of multiple factors. Comprehensive overviews of the application of DoE methods in combination with fuel cell analysis were presented by Wahdame et al. [42] and Karanfil [43].

For the present analysis, performing the parameter study in a full factorial way, i.e. testing all possible combinations of the four-dimensional parameter space with the factor levels shown in Table 2, would result in 17280 measuring points and is thus an unfeasible testing procedure. However, the number of experimental runs can be significantly reduced without loss of relevant information by applying DoE methods. The "D-optimal design" approach, i.e. a response surface methodology, seems well suited for planning the actual study, see e.g. [21,34,36]. This method is applied by using the software package Matlab R2021b as part of the Statistics and Machine Learning toolbox by calling the function `candexch()`, [44]. With D-optimal design it is possible to determine the most relevant parameter combinations after excluding certain combinations that cannot be attained as they would lead to e.g. fuel cell dry out or flooding. The limits of the parameter space are given in Table 3. The lower current density limit results from the discrete current density levels given in Table 2 and the minimum air blower frequency (≈ 400 Hz) together with the definition of a minimum cathode stoichiometry of 2 in order to avoid concentration losses, cf. [45]. The upper current density limit corresponds to a minimum cell voltage of 0.5 V. The upper stoichiometry limit is chosen to capture the effect where further increase of λ does not result in higher net power due to a disproportional increase of the blower power. The overall stack temperature limits are set to 55.0 ± 15.0 °C, where 55.0 °C is the mean stack temperature suggested by the manufacturer. However, to prevent dry out or flooding, the investigated temperature range is narrowed at the different pressure levels. More details about the parameter constraints and the derivation of the limits are given in Appendix B. Eventually, 480 parameter combinations yield an appropriate compromise between experimental effort and gain of knowledge for the present study.

The parameter configurations selected by the D-optimal design approach are based on a model equation, which has to be defined prior to the experiments. In this study, a polynomial model equation of the form

$$y(t,p,i,T,\lambda) = \alpha_0 + \alpha_1 t + \sum_{j=2}^{k} \alpha_j \; p^a \; i^b \; T^c \; \lambda^d \tag{1}$$

is chosen. The response variable is denoted by y. After performing the experiments, the model coefficients α are determined according to the choice of the response variable representing either the net power P_{net}, the average cell voltage U, or the relative humidity at the cathode outlet rH. The treatment factors are the runtime t, the chamber pressure p, the current density i, the stack temperature T, and the cathode stoichiometry λ. The exponents a, b, c, and d are selected to represent principal effects up to the fourth order, where one exponent is 1, 2, 3, or 4, and the others are 0. Interactions up to the third order are also included, meaning two, three, or all four exponents are 1, or one exponent is 1 and another is 2, with the remaining exponents being 0. With this choice of exponents, $k = 41$ and the total number of model coefficients including α_0 and α_1 is 42.

Note that the linear term for the runtime t in Eq. (1) accounts for a constant degradation rate. Interaction terms where t is multiplied with other treatment factors to account for e.g. current density or temperature depending degradation rates are beyond the scope of the present paper. A detailed analysis of the degradation behavior under low-pressure conditions will be given elsewhere.

3.3. Data evaluation

In this study, only steady-state measuring points according to the steady-state definition presented in Section 3.1 are considered. For determining the polarization curves measured at different ambient pressure levels shown in Section 4.1, only the part of descending current density is used as shown in Fig. 2. The fuel cell system's net power is determined by subtracting the parasitic power demand of the BoP components from the fuel cell gross power. The cell efficiency based on the lower heating value (LHV) of hydrogen, discussed in Section 4.2, is defined as, [7],

$$\eta = \frac{U}{1.254\ \text{V}}\ 100\ \%\,. \tag{2}$$

The software Stat-Ease 360 is used for the analysis of the parameter study, i.e. the estimation of the model coefficients α of Eq. (1) by the method of ordinary least squares [46]. Moreover, Stat-Ease 360 conducts an analysis of variance (ANOVA) and provides a detailed summary of the model's statistics, facilitating the identification of the best-fitting model for the experimental data.

The use of the D-optimal design requires the initial specification of a comprehensive model equation, i.e. Eq. (1), which is subsequently simplified by employing the principle of stepwise regression, particularly sequential backward selection. This method is applied by initially considering the complete model including all predictors and iteratively

Table 4
Measured average chamber pressure and the corresponding altitude according to [18] for the pressure levels investigated in Section 4.1.

Pressure level [hPa]	Avg. pressure [hPa]	Altitude [m]
1000	980	277
900	888	1101
800	789	2063
700	690	3123
600	589	4342
500	491	5712

dropping the least significant terms based on their statistical impact on the response variable [47]. After each removal, the model is re-estimated until only significant effects and interactions remain. The predictor significance is assessed by using the p-value with a threshold of 0.1, cf. [48].

For the regression evaluation, quantitative validation measures such as the adjusted and the predicted R^2 values [34] are employed alongside visual inspection. Specifically, the adjusted R^2 is used as metric to evaluate the model quality, as it accounts for the number of predictors relative to the sample size, thereby enabling a more precise evaluation of the model's performance.

Details about the regression models and their specifications including the ANOVA results are provided in Table 5 and in Appendix C.

For further information about the employed methods and procedures it is referred to Ref. [49].

4. Results and discussion

4.1. Experimental results using default control parameters at low-pressure operation

The following experimental results were determined at different pressure levels. During the experiments, the actual chamber pressures differed from the setpoints and the averaged pressure values together with the corresponding altitude according to [18] are listed in Table 4.

To quantify the performance losses of the PEMFC under test at low-pressure operation, polarization curve measurements are performed at different pressure levels (cf. Table 4) by keeping the temperature and stoichiometry control unchanged, cf. Table 1. The resulting polarization curves shown in Fig. 3a illustrate a strong effect due to the environmental pressure, which can be partly attributed to the accompanying lower oxygen partial pressure present at the electrode leading to a lower amount of reactants available for the electrochemical reaction, cf. [7]. While a low voltage drop due to the pressure reduction is observed at low current densities, the voltage drop with decreasing pressure is more pronounced at high current densities. This is due to enhanced mass transport losses under low-pressure conditions, [45]. A comparison of the polarization curves measured at 980 hPa and 491 hPa shows a cell voltage decrease of only 11 % at 0.2 A/cm^2, but a decrease of 27 % at 0.4 A/cm^2. As a result, the net power output also decreases significantly with decreasing pressure at high current densities, which is shown in Fig. 3b. The maximum power output at a pressure of 491 hPa is only 41 % of the maximum power at 980 hPa. A possible explanation for the unusual behavior observed at 0.4 A/cm^2 and the chamber pressures of 888 hPa and 789 hPa will be given in Section 4.5.

Note that at 500 hPa, Graf et al. [17] observed voltage drops of 4 % at 0.2 A/cm^2 and of 8 % at 0.4 A/cm^2 with respect to their measurements at 950 hPa by investigating the same fuel cell type as used in the present study. However, it has to be taken into account that the data presented in Ref. [17] represent dynamically observed current–voltage curves under low-pressure conditions, where each curve was measured within 300 s. Thus, the results should be compared with reservation.

The three main contributions to the parasitic power are the power demands of the air blower, the anode recirculation pump and the cooling pump. For the fuel cell system under test, the stack cooling is controlled by a bypass valve while the cooling pump runs at a constant speed, see Appendix A, Fig. A.13. Thus, the power demand of the cooling pump is constantly 102 W. Note that for net power optimization purposes, the cooling could also be controlled directly by adjusting the pump speed, avoiding or minimizing the use of a bypass valve. The power demands of the air blower and the anode recirculation pump at

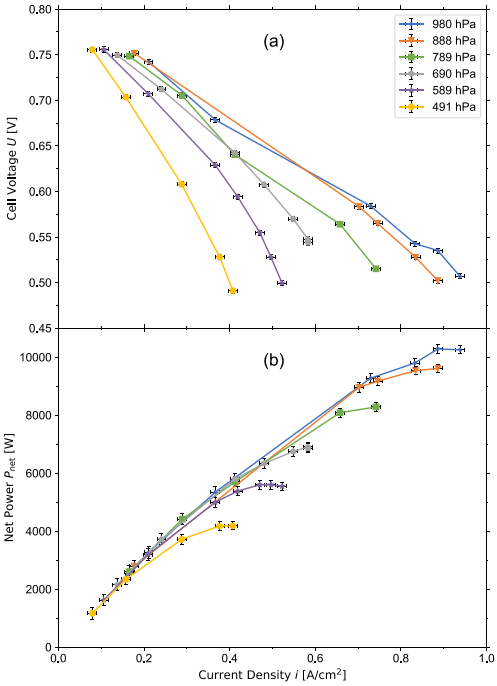

Fig. 3. Polarization curves (a) and net power (b) versus current density at different ambient pressure levels by using the default parameters for the stack temperature and cathode stoichiometry, see Table 1.

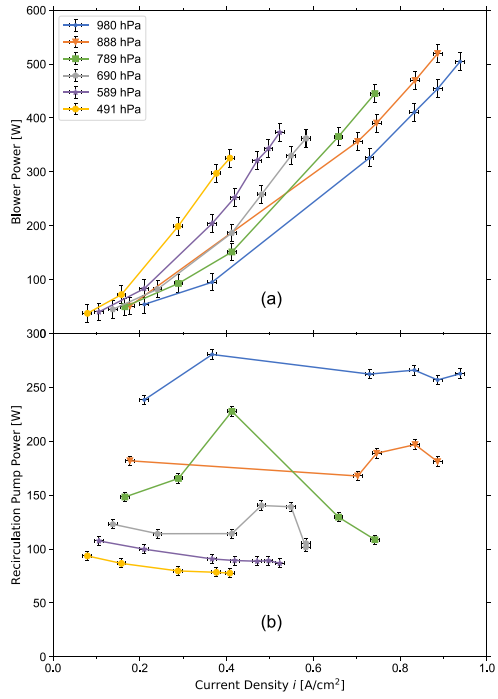

Fig. 4. Parasitic power demand of the air blower (a) and the recirculation pump (b) measured at different pressure levels and varying current densities.

different pressure and current density levels are shown in Fig. 4a and b, respectively. At all pressure levels the blower power demand rises with increasing current density as higher air flow rates are necessary for the electrochemical reaction, see Fig. 4a. In addition, the blower power demand increases significantly with decreasing pressure for a given current density. For example, at 0.4 A/cm^2, the power demand at 491 hPa increases by a factor of 2.9 compared to 980 hPa. This results from the fact that the blower is controlled to provide a certain cathode stoichiometry, i.e. a certain mass flow, at a given current density, cf. Table 1. Due to the decreasing density of air at low pressures, a higher blower speed and consequently a higher power is required to maintain the mass flow. Moreover, the low air density leads to a higher volume flow rate and thus to a higher pressure drop across the stack, which also results in a higher blower power demand. The anode recirculation pump is controlled by the Hydrogenics fuel cell controller, which aims to keep the pump at a constant speed. The required pump power strongly depends on the fluid density, which is primarily affected by the pressure. Thus, the power demand at low pressures decreases due to the low fluid density, see Fig. 4b. One should keep in mind that due to varying stack humidification, the anode fluid density can also change significantly as a result of the low density of hydrogen and the comparably high density of water vapor. This effect cannot be quantified due to the lack of anode humidity measurements but it is believed to be responsible for the changing power demand at different current densities for a given pressure in Fig. 4b, see e.g. the strong recirculation pump power increase at 789 hPa and $i = 0.4$ A/cm^2. The control approach of maintaining a constant speed combined with low fluid density at low pressures results in decreasing mass flow and may cause local fuel starvation. Thus, for aircraft applications, an adaptation to a constant mass flow at low-pressure operation could be a reasonable optimization approach. With this, the power demand of the recirculation pump would rise at low pressure levels, similar to the power demand of the air blower. However, with the default implemented control approach for the recirculation pump, the total parasitic power demand declines with decreasing pressure.

Fig. 5 shows the relative humidity rH measured at the cathode outlet versus the current density for various pressure levels. This gives an indication of the internal membrane humidification. Note that the results at 888 hPa were probably distorted by droplet formation on the probe, resulting in unrealistically high humidity values up to 92 %. With increasing current density, the relative humidity decreases at all pressure levels (except for 888 hPa) due to the rising stack temperature, cf. Table 1. For a given current density, the stack temperature, and therefore the saturation partial pressure, is the same at all pressure levels. However, the partial pressure of the gaseous water decreases with the ambient pressure, resulting in a low relative humidity, i.e. a drying effect. Proper water management is known to be crucial to fuel cell operation. Based on these results and the observation that the total parasitic power demand declines with decreasing pressure, it is assumed that the stack dehydration is a major cause of the severe power losses at low ambient pressures.

4.2. Regression model evaluation and identification of the optimal control parameters

Based on the results of the parameter study, model equations describing the response of the average cell voltage U, the system net power P_{net} and the relative humidity at the cathode outlet rH are derived by determining the corresponding coefficients α of the model Eq. (1), see Section 3.3. The exact values of the coefficients for each model equation used in the following evaluations are given in Appendix C. All results of response variables depending on the runtime t will be shown with values corresponding to the center of the experimental space at $t = 236$ h.

Optimization of the net power model $P_{\text{net}}(t, p, i, T, \lambda)$ yields the optimal stack temperature $T_{\text{opt}}(p, i)$ and optimal cathode stoichiometry

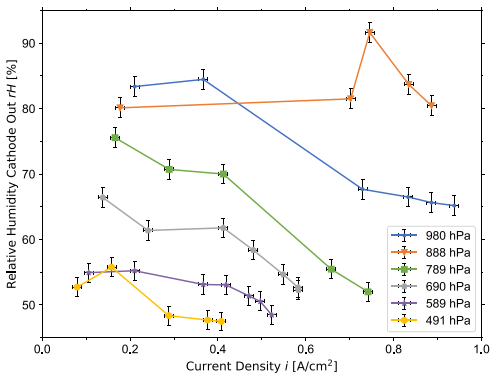

Fig. 5. Low-pressure effect on the relative humidity at the cathode outlet at varying current densities. The results at 888 hPa were probably distorted by droplet formation on the probe, leading to unrealistically high relative humidity values.

$\lambda_{\text{opt}}(p, i)$ to obtain the maximum net power for a given current density and ambient pressure, i.e. $P_{\text{net}}(t, p, i, T_{\text{opt}}, \lambda_{\text{opt}}) = \max\{P_{\text{net}}(t, p, i)\}$.

Fig. 6a shows the contour plot of the optimized net power model $P_{\text{net}}(t, p, i, T_{\text{opt}}, \lambda_{\text{opt}})$ at varying pressure and current density. The contour plots of $T_{\text{opt}}(p, i)$ and $\lambda_{\text{opt}}(p, i)$ are shown in Figs. 6c and d, respectively. Analyzing the highest achievable net power at 1000 hPa and at 500 hPa, in Fig. 6a, i.e. 10399 W and 5504 W, respectively, the power loss by using optimized control parameters is 47 %, compared to 59 % by using default control parameters as shown in Fig. 3b.

Evaluating the model of the relative humidity at the cathode outlet $rH(p, i, T, \lambda)$ with the optimal stack temperature and cathode stoichiometry, i.e. $rH_{\text{opt}}(p, i, T_{\text{opt}}, \lambda_{\text{opt}})$, yields the optimal stack humidification values shown in Fig. 6b. Note that the relative humidity turned out to be independent of the runtime, i.e. the corresponding term involving t was dropped in course of performing the procedure of sequential backward selection as described in Section 3.1. The optimal relative humidity at the cathode outlet is only slightly pressure-dependent but decreases with increasing current density. To achieve the desired cathode outlet humidity at a given current density value, strongly varying combinations of the stack temperature and cathode stoichiometry are identified as optimal values for different pressure levels in Fig. 6c and d, respectively. For example, to realize the optimal relative humidity of 59 % at $i = 0.5$ A/cm^2, the model yields $T_{\text{opt}} = 45.1$ °C, $\lambda_{\text{opt}} = 2.98$ for $p = 500$ hPa, and $T_{\text{opt}} = 64.3$ °C, $\lambda_{\text{opt}} = 2.55$ for $p = 989$ hPa.

The optimal stack temperature in Fig. 6c remains almost constant for a given pressure level. However, with decreasing pressure, the optimal stack temperature strongly decreases with a mean slope of 37 m°C/hPa, such that, in a first approximation, the optimal stack temperature follows the line of best fit

$$T_{\text{opt}}(p) = (26.5 + p\ 0.037/\text{hPa})\ [°\text{C}]\,. \tag{3}$$

This equation reflects, in a linear approximation, the dependence of the water saturation vapor pressure on the temperature. Thus, Eq. (3) can also be derived from the definition of the relative humidity as the ratio of water partial pressure (i.e. the product of the absolute pressure and the water mole fraction) and the water saturation vapor pressure. Therefore, a mean relative humidity of 60 % and a water mole fraction of 0.115 are used in conjunction with the Magnus equation [50] to express the temperature-dependent water saturation vapor pressure, which is then linearized around 46.0 °C.

The optimal stack temperature under low-pressure conditions shown in Fig. 6c is identified within the interplay between two opposing effects. On the one hand, a higher operating temperature positively affects the cell potential as it results in higher exchange current density, higher membrane conductivity and improved mass transport, [7]. On the other hand, a lower stack temperature, particularly together with

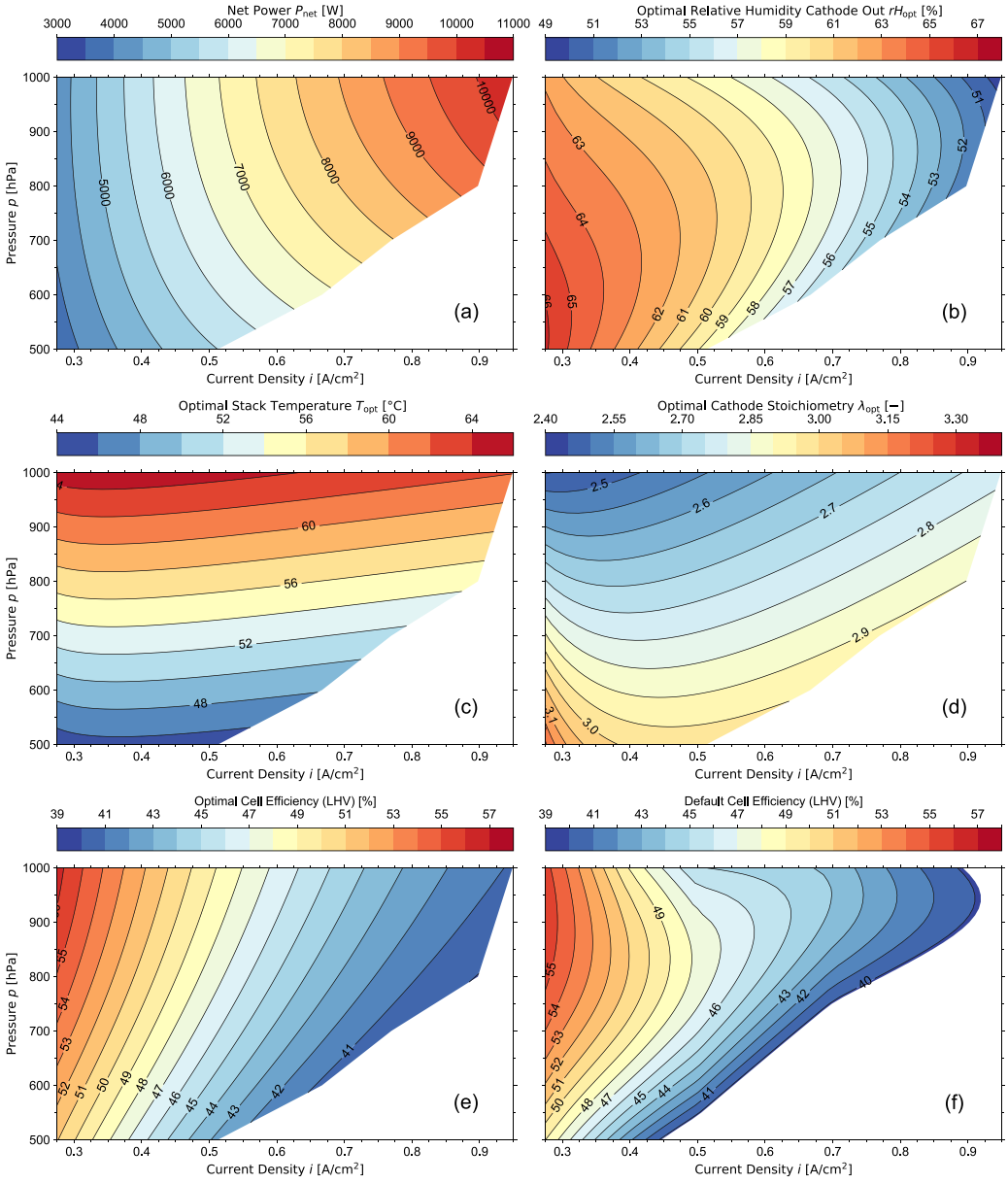

Fig. 6. Optimized net power model $P_{net}(t = 236\ \text{h}, p, i, T_{opt}, \lambda_{opt})$, (a), and optimal relative humidity model $rH_{opt}(p, i, T_{opt}, \lambda_{opt})$, (b), with the corresponding optimal control parameters for stack temperature $T_{opt}(p, i)$, (c), and cathode stoichiometry $\lambda_{opt}(p, i)$, (d). Cell efficiency η according to Eq. (2) based on the average cell voltage model $U(t = 236\ \text{h}, p, i, T, \lambda)$ evaluated with optimal control parameters, (e), and evaluated with default control parameters according to Table 1, (f).

increased cathode stoichiometry (see Fig. 6d), is required to guarantee optimal humidification of the fuel cell.

In Fig. 6d a clear trend towards higher cathode stoichiometry is visible at increasing current density and high pressure. At low pressure levels, the overall stoichiometry is higher while the values decrease with increasing current density, see also Fig. 7b. This is due to two counteracting effects: Higher stoichiometry results in a moderate pressurization of the stack and consequently to a slightly increased cell potential. However, higher stoichiometry also leads to increased blower power consumption. Therefore, optimizing the system net power yields optimal stoichiometry values that provide high pressurization to compensate for the low ambient pressure, but only moderately increase the blower power consumption. Note that for a detailed investigation of this matter, more information of the blower (Domel 793.3.285-517) including the compressor map with efficiency curves would be necessary.

Figs. 6e and f show the cell efficiency η [cf. Eq. (2)] based on the average cell voltage model $U(t, p, i, T, \lambda)$ (see Appendix C.2) evaluated with optimized and default control parameters, respectively. While in Fig. 6e the model results are shown according to the investigated constrained parameter space (see Appendix B), in Fig. 6f only results with $U \geq 0.5$ V (i.e. $\eta \geq 39.9$ %), representing the validity limit of the model, are depicted. The parameter optimization shows a significant efficiency increase at all pressure levels in comparison with the cell efficiency obtained with default control parameters. At high pressure levels, the efficiency is particularly increased at high current density values. At low pressure levels, the parameter optimization leads to higher overall efficiency as well as a less pronounced efficiency decrease with rising current density.

In Figs. 7a and b the optimized parameters for stack temperature and cathode stoichiometry control are shown as isobars for the investigated pressure levels between 1000 and 500 hPa. For comparison, the default parameters given by the manufacturer are shown as dashed lines, see also Table 1. The optimized parameters deviate strongly from the default parameters both quantitatively and qualitatively, even for 1000 hPa, which is about the fuel cell system's design pressure

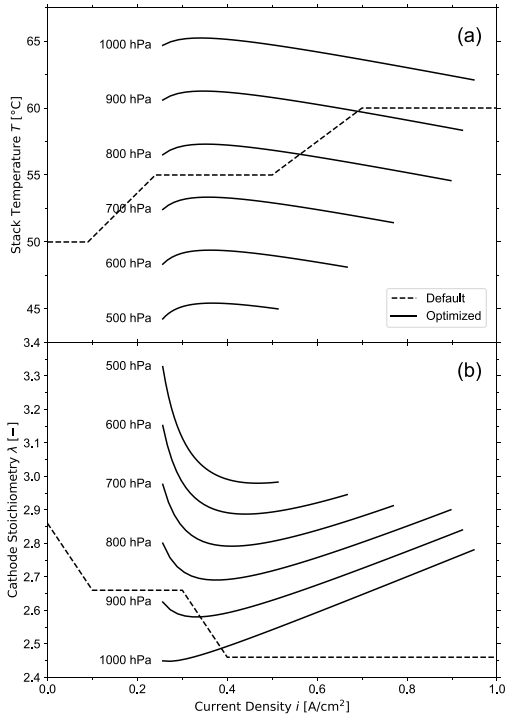

Fig. 7. Stack temperature (a) and cathode stoichiometry (b) control parameters versus current density. Isobars of the optimized parameters are shown as solid lines. The default parameters according to Table 1 are shown as dashed lines.

of 989 hPa [29]. Whereas the default control strategy (dashed lines) requires to increase the stack temperature and decrease the stoichiometry with rising current density, the optimized parameters show rather inverse characteristics, see the solid curves for 1000 hPa.

4.3. Regression model validation

To validate the regression models presented in the previous section, polarization curves are recorded at p = 978 hPa and p = 497 hPa using control parameters for the stack temperature and the cathode stoichiometry close to the identified optimal control parameters shown in Fig. 7. Note that the fuel cell controller of the fuel cell system under test allows to set the cathode stoichiometry with a precision of 0.1, thus the optimal values suggested by the model cannot be attained exactly. Therefore, the predictions of the cell voltage model $U(t, p, i, T, \lambda)$, the net power model $P_{\text{net}}(t, p, i, T, \lambda)$ and the relative humidity model $rH(p, i, T, \lambda)$ are compared to the experimental data of the polarization curve measurements by using the exact same values of T and λ for the models as applied for the experimental measurements. Furthermore, all experimental data presented in the following are degradation corrected to improve the comparability with the model. To this end, the center of the experimental space at t = 236 h is chosen as the common time instant. This means that the measured values of P_{net} and U are adjusted by applying the corresponding coefficients of the model Eq. (1), accounting for the linear degradation, i.e. α_1. A constant voltage loss rate of −77 µV/h and a constant net power loss rate of −847 mW/h are identified as coefficient α_1 for the voltage and the net power model, respectively [see Appendix C, Eqs. (C.1) and (C.2)]. Considering that the model equations are only valid within the investigated boundaries given in Table 3, the models are only compared with experimental data lying within the validity region, i.e. within the current density limits.

Fig. 8a shows the prediction of the cell voltage model $U(t, p, i, T, \lambda)$ in comparison to the validation measurements. Based on the testing

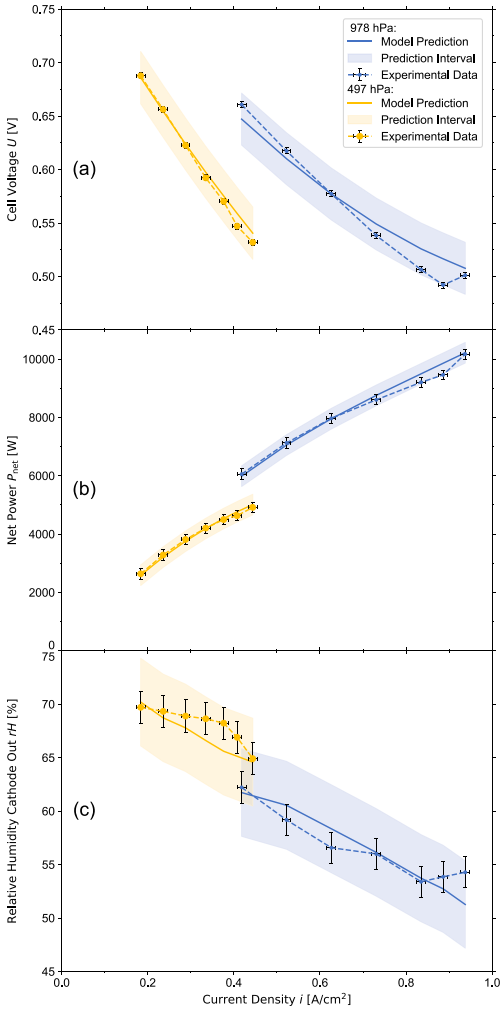

Fig. 8. Validation of the cell voltage model $U(t = 236\ \text{h}, p, i, T, \lambda)$, (a), the net power model $P_{\text{net}}(t = 236\ \text{h}, p, i, T, \lambda)$, (b), and the relative humidity model $rH(p, i, T, \lambda)$, (c). The model predictions including the prediction intervals with a confidence level of 95 % indicated by the shaded areas are compared to experimental measurements at the pressure levels 978 hPa (blue) and 497 hPa (yellow).

procedure for the parameter study (see Section 3.1), the model is only valid for the ascending part of the polarization curve and hysteresis effects cannot be represented by the model. Thus, the experimental data shows the ascending part of the polarization curve measurements, cf. the solid line in Fig. 2. At both pressure levels, the experimental data shown in Fig. 8a is well within the model prediction interval with a confidence level of 95 %, indicated by the shaded area.

Even though the experimental data shown in Fig. 8a are degradation corrected (cf. Section 3.2), the model predicts a notably higher cell voltage at high current density at both pressure levels compared to the validation experiment, which reveals possible limitations of the model. First, this indicates that concentration losses are underrepresented by the model, which would suggest the use of a physical-empirical model equation. Another explanation for the deviation at high current density may be that considering a constant voltage loss rate is not sufficient to capture the full degradation behavior and a current density-dependent voltage loss rate as found by Ref. [51] should be included into the model equation. Note that a methodically accurate incorporation of treatment factor-dependent degradation requires to initially include the interaction between the runtime and all treatment factors and then identify the most relevant interactions by performing sequential

Table 5
Fit statistics of the validated models.

Model	RMSE	Mean	C.V. %	PRESS	R^2	Adj. R^2	Pred. R^2	Adeq. Prec.
$U(t,p,i,T,\lambda)$	0.0121	0.5862	2.07	0.0764	0.9835	0.9824	0.9810	103.50
$P_{net}(t,p,i,T,\lambda)$	176.66	5946	2.97	1.59×10^7	0.9951	0.9949	0.9945	210.88
$rH(p,i,T,\lambda)$	2.05	59.19	3.46	2245.6	0.9605	0.9585	0.9537	82.42

backward selection. The evaluation and physical interpretation of the remaining interactions would require a more comprehensive measurement setup including e.g. electrochemical impedance spectroscopy or cyclic voltammetry, cf. [52]. This is beyond the scope of the present study and may be investigated in the future. However, the use of a constant degradation rate yields significantly higher model accuracy compared to completely neglecting degradation. For example, while a cell voltage model without degradation term exhibits a root mean square error (RMSE) of 13.2 mV, the inclusion of the linear degradation term yields a RMSE of 12.1 mV, which reduces the coefficient of variation (C.V.) from 2.24 % to 2.07 % (see Table 5). Similarly, the RMSE of the net power model reduces from 186.61 W without degradation term to 176.66 W by including the term, i.e. a reduction of C.V. from 3.14 % to 2.97 %.

In Fig. 8b the net power model prediction at both pressure levels is in good agreement with the measurement data. Note that the optimal stack temperature model $T_{opt}(p,i)$ and the optimal cathode stoichiometry model $\lambda_{opt}(p,i)$ are derived from the net power model, see Section 4.2. Thus, a separate validation of these two models is omitted.

In Fig. 8c the relative humidity model $rH(p,i,T,\lambda)$ is compared to the measured relative humidity at the cathode outlet. For both p = 978 hPa and p = 497 hPa, the validation measurements are in good agreement with the model prediction and within the shaded prediction interval with a confidence level of 95 %.

In Table 5 key fit statistics of the validated models including the RMSE, the C.V., the adjusted and predicted R^2, etc. are summarized. All models exhibit excellent goodness of fit with adjusted R^2 values > 0.95 and low C.V. values, indicating high prediction accuracy. Furthermore, the predictive R^2 values are close to the adjusted R^2, confirming good generalizability without overfitting, [48]. The adequate precision values are far above the recommended threshold of 4, [34], demonstrating strong signal-to-noise ratios across all models. The ANOVA of all validated models can be found in Appendix C.

4.4. Net power sensitivity analysis

A response variable's sensitivity to parameter changes can be analyzed by means of a perturbation plot. There, the effect of single parameter variations from a chosen reference point is visualized, while all other parameters are assumed to be fixed (one-factor-at-a-time). Factor curves with a steep slope or strong curvature show that the response variable is very sensitive to that particular factor change. Since the net power was chosen as target value to identify the optimal operating parameters, the net power model is analyzed in terms of sensitivity to parameter variations in the following. In Figs. 9 and 10 solid curves represent the investigated constrained parameter range for the shown reference point. Dotted lines indicate the overall parameter range investigated in course of the parameter study, cf. Table 3.

In Fig. 9 the approximate center of the investigated parameter space (t = 236 h, p = 750 hPa, i = 0.51 A/cm^2, T = 55 °C, λ = 2.8) is chosen as reference point. Based on the slope, the most significant factor is the current density (green curve) followed by the pressure (black curve). While the strong dependence of the net power on the current density is not surprising due to the direct implications of the current density on the gross power, the strong pressure sensitivity underlines the significance of the pressure related optimization effort of the present study. In terms of the two control parameters T and λ, changes of the stack temperature are more significant with a distinct

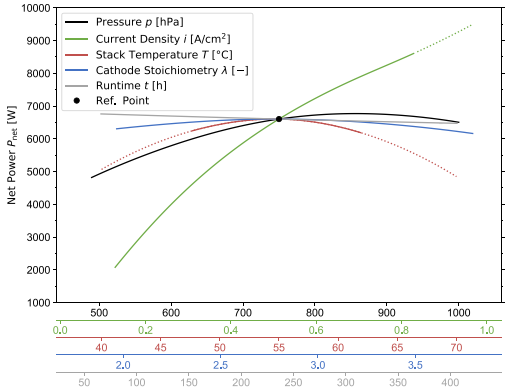

Fig. 9. Perturbation plot of the net power model $P_{net}(t,p,i,T,\lambda)$. The reference point corresponds to the approximate center of the investigated parameter space, i.e. t = 236 h, p = 750 hPa, i = 0.51 A/cm^2, T = 55 °C, λ = 2.8. Each horizontal axis corresponds to the line shown in the same color.

optimum value compared to changes of the cathode stoichiometry, which is in agreement with the observations by Werner et al. [21].

In Figs. 10a and b the perturbation plots of the net power are shown with i = 0.25 A/cm^2 and i = 0.75 A/cm^2, respectively. All other factors correspond to the approximate center of the investigated parameter space, cf. Fig. 9. Analyzing the sensitivity at a low current density in Fig. 10a shows small slopes and curvatures of the factor curves, indicating that the net power is equally (in-)sensitive to all factors. This implies that the fuel cell system's net power at low current densities is relatively robust without a high potential for optimization through control parameter optimization. However, the opposite can be observed in Fig. 10b, where the sensitivity of the net power at high current density is shown. Here, small parameter variations lead to strongly changing net power responses. This behavior supports the significance of the above identified optimal parameters, particularly for reaching high net power at high current density.

A net power sensitivity analysis at high and low pressure values yields the same level of parameter sensitivity across the whole pressure range, with analog observations as in Fig. 9. A separate discussion of the sensitivity at different pressure levels is therefore omitted.

4.5. Optimal control strategy for low-pressure operation

Operating the fuel cell system under low-pressure conditions by applying the optimal parameters for stack temperature and cathode stoichiometry control as identified in Section 4.2 (see Figs. 6c and d, or Fig. 7) yields a significantly higher net power output compared to operating the system with the default control parameters according to Table 1.

In Fig. 11a the maximum net power obtained by evaluating the model $P_{net}(t,p,i,T,\lambda)$ with optimal and default control parameters at varying pressure is shown as red solid and black dashed lines, respectively. The net power measurements obtained with default control parameters (black squares) are within the prediction interval of the corresponding model, whereas the net power measurements obtained with control parameters close to the optimal values (red dots) lie slightly below the model prediction using the exact optimal control parameters. Considering the good agreement of the validation results in Fig. 8, where the model results and the measurements are obtained by applying identical control parameters, it seems that the small deviation from the optimal parameter values (due to the fuel cell controller allowing to set the stoichiometry only with a precision of 0.1) result in noticeable performance losses. This is in accordance with the sensitivity

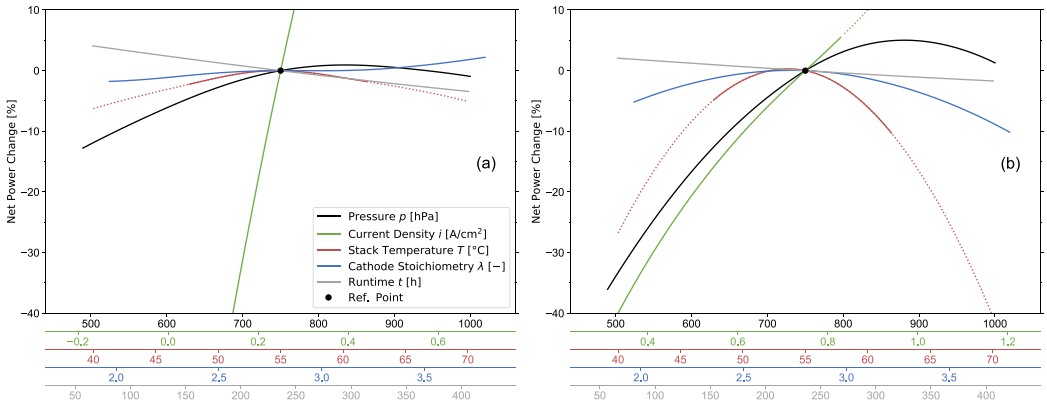

Fig. 10. Perturbation plots of the net power model $P_{\text{net}}(t, p, i, T, \lambda)$. The reference points of all subfigures correspond to $t = 236$ h, $p = 750$ hPa, $T = 55$ °C, $\lambda = 2.8$, (a): $i = 0.25$ A/cm^2; (b): $i = 0.75$ A/cm^2. Each horizontal axis corresponds to the line shown in the same color.

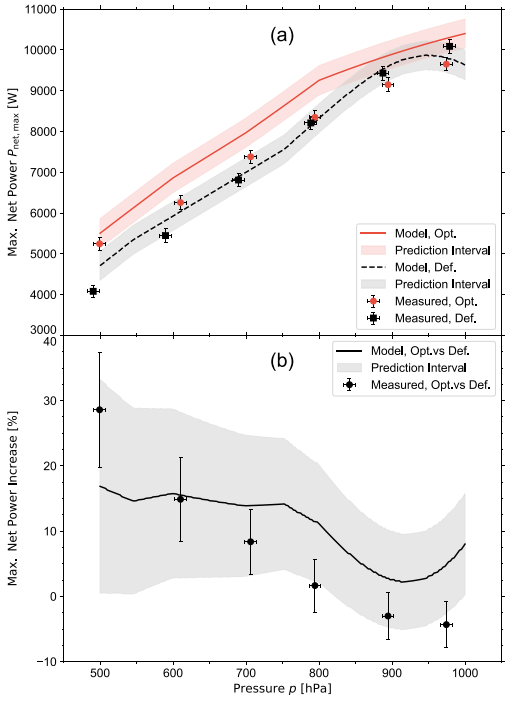

Fig. 11. Comparison of the maximum net power at different pressure levels, (a). The model predictions $P_{\text{net}}(t = 236\text{ h}, p, i, T, \lambda)$ are shown as red solid line with $T_{\text{opt}}(p, i)$ and $\lambda_{\text{opt}}(p, i)$, and as black dashed line with default parameters. The red dots and black squares show the experimentally obtained maximum net power using parameters as close as possible to $T_{\text{opt}}(p, i)$ and $\lambda_{\text{opt}}(p, i)$, and default parameters, respectively. Relative maximum net power increase comparing the model predictions and comparing the measured values, (b). All shaded areas represent model prediction intervals with a confidence level of 95 %. All experimental data is degradation corrected and shown for $t = 236$ h.

analysis of the net power at high current densities in Section 4.4. However, the reduced performance may also be partly attributed to the observations in Figs. 8a and b, where the model prediction overestimates the performance at high current density compared to the experimental data, indicating reduced model capability to accurately capture concentration losses and enhanced degradation at high current density. This effect is particularly evident when comparing the experimental data at $p > 800$ hPa. There, the current density-dependent degradation adherent to the data obtained with optimized parameters (red dots), which was measured at the end of the test campaign (after > 415 h of operation), seems to be larger than the net power gain due to parameter optimization. Consequently, the overall power output is lower than by using default parameters at the beginning of the test campaign (black squares). From these observations it is assumed that accelerated degradation has taken place due to strongly varying stack humidification as well as rapid load changes during the measurements. However, a detailed degradation analysis is beyond the scope of the present study.

In Fig. 11b the relative increase of the maximum net power by applying optimal control parameters is shown for both model (line) and experimental (dots) results. The relatively large prediction interval shown as shaded area as well as the large measurement uncertainties result from consequent error propagation. While low to moderate performance increase can be observed at high pressure levels, a strong increase appears under low-pressure conditions. The model predicts the highest relative net power increase at $p = 500$ hPa with 17 % (i.e. 791 W) performance improvement. The optimization potential under low-pressure conditions can be confirmed by the comparison of the experimental results. At a pressure of 497 hPa, the experimental data show a relative net power increase as high as 29 % (i.e. 1167 W). Considering the uncertainties of the model and the experiment, both results are consistent.

It is well known that maintaining a fuel cell in optimal humidification conditions is crucial for high performance as well as durability. In Fig. 12 the optimal relative humidity at the cathode outlet predicted by the regression model $rH_{\text{opt}}(p, i, T_{\text{opt}}, \lambda_{\text{opt}})$ is shown for the six investigated pressure levels between 1000 and 500 hPa. The prediction intervals are indicated by the shaded areas shown in the same color as the corresponding model prediction curves. Remarkably, the prediction curves lie almost on top of each other. Moreover, they lie within each other's prediction intervals. This indicates that the optimal relative humidity at the cathode outlet is pressure-independent and, to a first approximation, follows the black dashed line of best fit

$$rH_{\text{opt}}(i) = (70.9 - i\ 20.7\ \text{cm}^2/\text{A})\ [\%]\,. \tag{4}$$

For comparison, the relative humidity measured at the cathode outlet during experiments with control parameters set as close as possible to the optimal values $T_{\text{opt}}(i, p)$ and $\lambda_{\text{opt}}(i, p)$, are shown as colored markers in Fig. 12. The majority of the measurement data lies within the prediction intervals but slightly below the model prediction curves. This may be due to the fact that the fuel cell controller does not allow to set the exact optimal parameter values. Nevertheless, all measurement points follow a clear trend towards a lower relative humidity at higher current density.

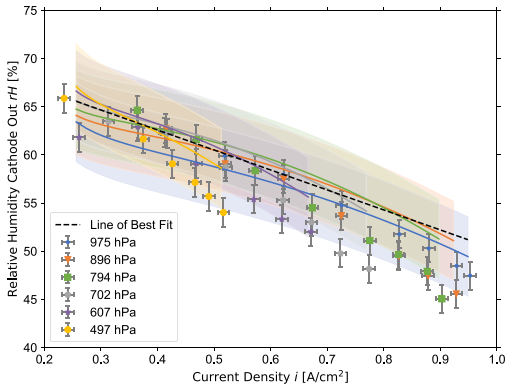

Fig. 12. The solid lines show the predicted optimal relative humidity $rH_{opt}(p, i, T_{opt}, \lambda_{opt})$ for $p = 500$ hPa (yellow), for $p = 600$ hPa (violet), for $p = 700$ hPa (gray), for $p = 800$ hPa (green), for $p = 900$ hPa (orange) and for $p = 1000$ hPa (blue). The model prediction intervals with a confidence level of 95 % are indicated by the area shaded in the corresponding color. The black dashed line of best fit approximates the trend of all shown model prediction curves according to Eq. (4). The experimental data is obtained by applying control parameters as close as possible to $T_{opt}(i, p)$ and $\lambda_{opt}(i, p)$.

The identification of the optimal relative humidity yields a possible explanation for some unusual behavior observed when the PEMFC is operated under low-pressure conditions with default control parameters. In Fig. 3a and b the performance at $i = 0.4$ A/cm^2 and a chamber pressure of 888 hPa and 789 hPa are almost identical. The application of the default parameters for stoichiometry and temperature control leads to relative humidity values of 70 % and 62 % for 888 hPa and 789 hPa, respectively, see Fig. 5. According to Eq. (4), $rH_{opt}(0.4\ \text{A/cm}^2) = 61.7$ %. This shows that the results in Fig. 3 at $i = 0.4$ A/cm^2 and 789 hPa are obtained with an optimally humidified fuel cell, whereas a too wet fuel cell at $i = 0.4$ A/cm^2 and 888 hPa leads to significant performance losses.

Finally, a simplified control strategy yielding high system net power at low-pressure operation could be implemented by controlling the pressure-dependent stack temperature according to Eq. (3). On the other hand, the cathode stoichiometry is used to maintain the relative humidity at the cathode outlet in its current density-dependent optimal state according to Eq. (4) with an accuracy of about ±5 %. However, to achieve the highest possible net power, the stack temperature and the cathode stoichiometry have to be set according to $T_{opt}(p, i)$ and $\lambda_{opt}(p, i)$ in Figs. 6c and d, respectively, see also the model Eqs. (C.4) and (C.5) in Appendix C.

The presented control functions are limited to the application to the fuel cell system under test. However, the proposed optimization framework consisting of a DoE based characterization of the PEMFC system followed by the derivation of model equations and the optimization regarding net power, which ultimately yields the optimal control functions, provides a generic procedure applicable to various other fuel cell systems with a comparable setup. This means a non-pressurized, liquid-cooled, self-humidifying fuel cell system such that the treatment factors are identical to the present investigation.

5. Conclusions

This study investigated the challenges of operating a PEMFC system under low ambient pressure conditions by operating a Hydrogenics HyPM HD 10-120 stack inside a low-pressure chamber. Across a pressure range from 980 and 491 hPa (simulating altitudes up to 5712 m), a net power loss of up to 59 % was observed when operating with the manufacturer's default parameters for stack temperature and cathode stoichiometry control. The performance degradation was attributed to increased parasitic losses from the BoP systems and to membrane drying due to reduced water partial pressure.

To identify the optimal operating conditions in terms of system net power, a comprehensive parameter study was performed by applying statistical DoE methods. In course of the parameter study, the stack temperature and the cathode stoichiometry were varied at different current density and chamber pressure levels. Based on the experimental results, model equations were derived for the cell voltage $U(t, p, i, T, \lambda)$, the net power $P_{net}(t, p, i, T, \lambda)$ and the relative humidity at the cathode outlet $rH(p, i, T, \lambda)$. The models' prediction capabilities were confirmed by the comparison with validation measurements. Optimization of the net power model yielded the optimal control functions $T_{opt}(p, i)$ and $\lambda_{opt}(p, i)$. The experimental application of these optimal parameters resulted in a significantly higher performance at low-pressure operation compared to the use of the default parameters. At 497 hPa, a maximum net power gain of 29 % could be reached.

Importantly, the analysis revealed two simplifying trends: Firstly, the optimal stack temperature decreases linearly with pressure and is approximately independent of current density. Secondly, the optimal relative humidity decreases linearly with current density and is independent of pressure. These findings led to a novel, simplified pressure- and load-adaptive control strategy. Therefore, the linear relation for $T_{opt}(p)$ is applied, while the stoichiometry is varied to maintain the optimal humidification $rH_{opt}(i)$. Compared to previous studies that examined isolated parameter effects or fixed pressure levels, this work delivers an experimentally validated and practically implementable continuous solution for net power maximization under low-pressure conditions. This contributes a significant advancement to the field of altitude-adaptive PEMFC control by providing a generalizable optimization framework applicable to various other fuel cell systems exhibiting a comparable setup.

6. Future research

The present study indicates considerable optimization potential through environmental pressure-dependent temperature and stoichiometry control, without significant additional power requirements. The results might also be transferable to the operation of pressurized fuel cells at high altitudes. Applying the proposed optimization approach to such systems could lead to an operation with reduced pressurization requirements for a given power output at a given ambient pressure. As a consequence, a lighter and smaller compressor could be used, causing less parasitic power loss and leading to a higher specific power density of the PEMFC system.

Aiming at high-altitude operation of PEMFC systems for aviation applications, it is planned to take into account the effect of low ambient temperature additionally to low pressure in further investigations. Moreover, the present study showed that more sophisticated, e.g. physical-empirical, model equations including operating parameter depending degradation should be considered in future studies.

CRediT authorship contribution statement

Dominik Murschenhofer: Writing – original draft, Supervision, Resources, Project administration, Methodology, Investigation, Formal analysis, Conceptualization. **Jonas Settele:** Visualization, Validation, Software, Methodology, Investigation, Formal analysis, Data curation. **Cornelie Bänsch:** Writing – review & editing, Conceptualization.

Declaration of competing interest

The authors declare that they have no known competing financial interests or personal relationships that could have appeared to influence the work reported in this paper.

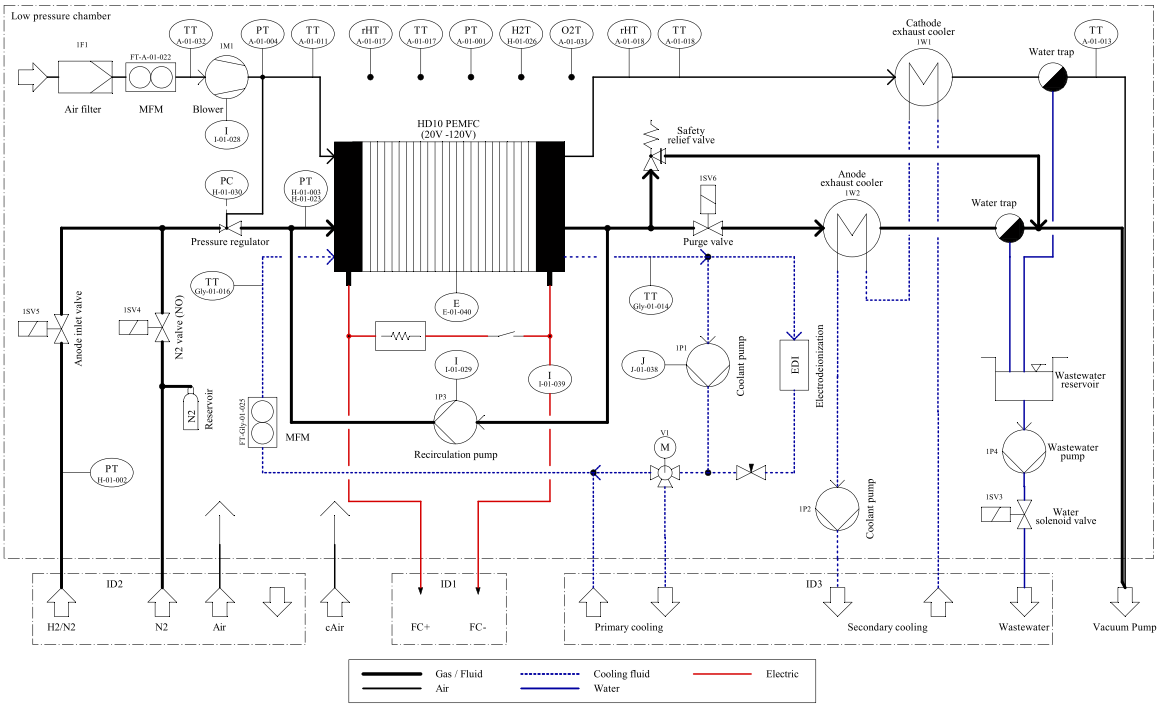

Fig. A.13. Piping and instrumentation diagram of the inside of the ATLAS low-pressure chamber.

Acknowledgments

Funding of the project EnaBle (20M1905) by the German Federal Ministry for Economic Affairs and Energy is gratefully acknowledged. Moreover, the authors should like to thank Fabian Krauth for his support during the test campaign and Pascal Meier, Oliver Thalau and Patrick Stehle for many helpful discussions concerning test procedures, evaluation and testbed adaption. Finally, the authors thank the anonymous reviewers for their comments, which helped to improve the quality of the paper.

Appendix A. ATLAS testbed: Piping and instrumentation

See Figs. A.13 and A.14 and Table A.6.

Appendix B. Parameter constraints

In course of the parameter study, preliminary pilot experiments identified certain unattainable parameter combinations, as they would lead to fuel cell dry out or flooding. The range of stable operating conditions was determined based on the relative humidity at the cathode outlet, which was found to be between 48 % and 95 %.

Assuming a negligible water content at the fuel cell inlet, Eq. (6-69) proposed by [7], can be used to determine the relative humidity at the cathode outlet, i.e.

$$rH = \frac{2r_{O2}}{\lambda + r_{O2}} \frac{p_{out}}{p_{sat}(T_{out})}, \tag{B.1}$$

where r_{O2}, p_{out} and $p_{sat}(T_{out})$ denote the oxygen concentration at the cathode inlet, the pressure at the cathode outlet and the saturation vapor pressure as function of the cathode outlet temperature, respectively.

Using Eq. (B.1), the corresponding saturation pressure range can be determined for the upper and lower relative humidity boundaries across all cathode stoichiometry and pressure levels. To this end, it is assumed that the exhaust gas temperature at the cathode outlet corresponds to the stack temperature. According to the International Association for the Properties of Water and Steam (IAPWS) [53], the saturation pressure can thus be directly related to the stack temperature limits.

Since the range of achievable humidity levels decreases with increasing current density due to flooding, the relative humidity at the cathode outlet is limited to 80 % for the maximum current density at each pressure level (see the back surface in Fig. B.15). Additionally, the overall stack temperature limits are set to 55.0 ± 15.0 °C, where 55.0 °C is the mean stack temperature suggested by the manufacturer. The discussed constraints result in the detailed parameter limitations presented in Fig. B.15.

Appendix C. Regression model equations and ANOVA

In all following model equations, the units of the model coefficients are omitted. However, the model parameters t, p, i, T and λ should be applied with their corresponding units [s], [hPa], [A/cm^2], [°C] and [–], respectively.

C.1. Net power model $P_{net}(t, p, i, T, \lambda)$

After dropping non-significant terms by sequential backward selection, the net power model equation reads:

$$\begin{aligned} P_{net}(t,p,i,T,\lambda) = (&8861.76748 - 0.84719 \cdot t + 13.76083 \cdot p - 46379.64961 \cdot i \\ &- 361.86707 \cdot T - 2723.52955 \cdot \lambda - 57.44845 \cdot pi \\ &- 0.31631 \cdot pT - 1.61862 \cdot p\lambda + 2236.65666 \cdot iT \\ &+ 16855.38278 \cdot i\lambda + 44.22505 \cdot T\lambda + 0.00529 \cdot p^2 \\ &- 13930.37965 \cdot i^2 + 4.15703 \cdot T^2 + 281.45122 \cdot \lambda^2 \\ &+ 1.75750 \cdot piT + 8.30920 \cdot pi\lambda - 263.04016 \cdot iT\lambda \\ &- 0.03997 \cdot p^2 i + 7.96305 \cdot pi^2 - 179.06403 \cdot i^2 T \\ &- 24.57336 \cdot iT^2 - 1582.07426 \cdot i\lambda^2 + 6721.41114 \cdot i^3) \text{ [W]}. \end{aligned} \tag{C.1}$$

The net power model's ANOVA is given in Table C.7, while the model's fit statistics is given in Table 5.

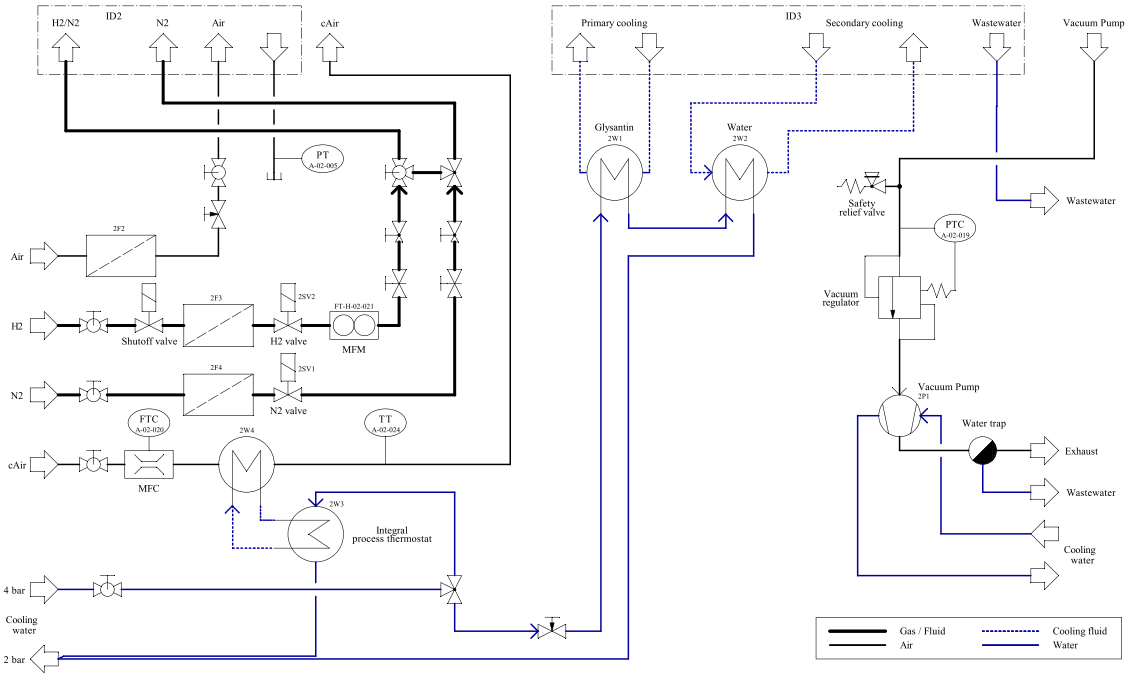

Fig. A.14. Piping and instrumentation diagram of the outside of the ATLAS low-pressure chamber.

Table A.6
List of the implemented sensors of the ATLAS testbed, including the reference code used in the piping and instrumentation diagrams (P&ID) of Figs. A.13 and A.14, and the measuring range and error of the sensors. While the unit slpm denotes standard liter per minute referenced to 1013 hPa at 21 °C, the unit ln/min refers to 1013 hPa at 0 °C. Some sensor measuring errors are based on the full scale (FS), while others are based on the measured value (MV).

P&ID code	Measured value [unit]	Type	Manufacturer	Measuring range	Measuring error
E-01–040	Cell pair voltage [V]	LTC6803–1	Linear Technology Corp.	−0.3 – 5 V	±2.8 mV
FT-A-01–022	Cathode air flow in [slpm]	AFH10-02 (OEM: 800-01262)	Hitachi Astemo Americas Inc.	–	–
FT-Gly-01–025	Coolant flow [l/min]	Typ 210 DN20	Huba Control AG	5 – 85 l/min	< ±1 % FS
FT-H-02–021	Hydrogen volume flow [ln/min]	EL-FLOW Select F-112AC	Bronkhorst GmbH	1.4 – 200 ln/min	±0.5% MV ±0.1 % FS
FTC-A-02–020	Chamber air flow [ln/min]	MFC D-6381-DR/003AI	Bronkhorst GmbH	100 – 5000 ln/min	±1.0% MV ±0.5 % FS
H2T-H-01–026	H_2 content [ppm]	PowerKnowz	Neodym Technologies Inc.	0 – 20000 ppm	±800 ppm
I-01–028	Current air blower [A]	DK 20 C420 U	LEM International SA	0 – 20 A	±1 % FS
I-01–029	Current recirculation pump [A]	DK 20 C420 U	LEM International SA	0 – 5 A	±1 % FS
I-01–039	Stack current [A]	DCS36-200-1	InPower Electronics	0 – 200 A	±1 % FS
J-01–038	Water pump power [W]	WP29 24V	EMP Corp.	0 – 360 W	–
O2T-A-01–031	O_2 content [Vol%]	MF010-O-LC	Dittrich Elektronic GmbH	0.1 – 25 Vol%	±1.5 % FS
PT-A-01–004	Pressure cathode in [hPa]	DRTR-ED-20MA-A2B	B+B Thermo-Technik GmbH	0 – 2 bar(a)	< ±0.4 % FS
PT-A-02–005	Chamber pressure [hPa]	DRTR-ED-20MA-A5B	B+B Thermo-Technik GmbH	0 – 5 bar(a)	< ±0.4 % FS
PT-H-01–001	Chamber pressure [hPa]	DRTR-ED-20MA-A2B	B+B Thermo-Technik GmbH	0 – 2 bar(a)	< ±0.4 % FS
PT-H-01–002	Pressure H_2 supply [hPa]	DRTR-ED-20MA-A10B	B+B Thermo-Technik GmbH	0 – 10 bar(a)	< ±0.4 % FS
PT-H-01–003	Pressure anode [hPa]	DRTR-ED-20MA-A2B	B+B Thermo-Technik GmbH	0 – 2 bar(a)	< ±0.4 % FS
PT-H-01–023	Pressure anode internal [hPa]	AST4000FV0025P4A1000	American Sensor Technologies	−14.7 – 25 PSI	< ±0.5 % FS
PTC-A-02–019	Chamber pressure regulator [bar]	RPD200/0-1abs./3/a/1/N	Drumag GmbH	0 – 1 bar(a)	< ±0.2 % FS
TT-A-01–011	Temp. cathode in [°C]	Thermocouple Type K	ES Electronic Sensor GmbH	−50 – 200 °C	±1.5 °C
TT-A-01–012	Resistor temp. [°C]	Thermocouple Type K	ES Electronic Sensor GmbH	−50 – 200 °C	±1.5 °C
TT-A-01–013	Temp. intercooler out [°C]	Thermocouple Type K	ES Electronic Sensor GmbH	−50 – 200 °C	±1.5 °C
TT-A-01–017	Chamber temp. [°C]	KS-CAN-03	ZILA GmbH	−40 – 80 °C	±0.5 °C
TT-A-01–018	Temp. cathode out [°C]	EE33-MFT J2022HV01/AB6-T12	E+E Electronik GmbH	−40 – 120 °C	±0.2 °C
TT-A-01–032	Temp. air blower in [°C]	PT1000 (DIN B)	Otom Group GmbH	−60 – 180 °C	±(0.3 + 0.005MV) °C
TT-Gly-01–014	Coolant temp. stack out [°C]	PT1000 (DIN A)	Otom Group GmbH	−60 – 180 °C	±(0.15 + 0.002MV) °C
TT-Gly-01–016	Coolant temp. stack In [°C]	PT1000 (DIN B)	Huba Control AG	−40 – 125 °C	±0.3 °C
rHT-A-01–017	Relative humidity chamber [%]	KS-CAN-03	ZILA GmbH	0 – 100 %	±2 %
rHT-A-01–018	Relative humidity cathode out [%]	EE33-MFT J2022HV01/AB6-T12	E+E Electronik GmbH	0 – 100 %	±(1.3 + 0.3%MV) %
	Auxiliary Power Supply [V]	PS 8160-60 2U	Elektro-Automatik GmbH	0 – 160 V	< ±0.2 % MV

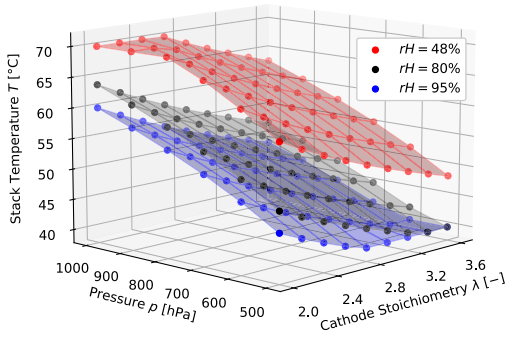

Fig. B.15. Detailed parameter limits for the stack temperature and the cathode stoichiometry used in course of the parameter study at different pressure levels. The red surface represents the limits that apply to obtain minimal relative humidity values at the cathode outlet of 48 %. The black and blue surfaces represent the limits that apply to obtain maximum relative humidity values of 80 % and 95 %, respectively.

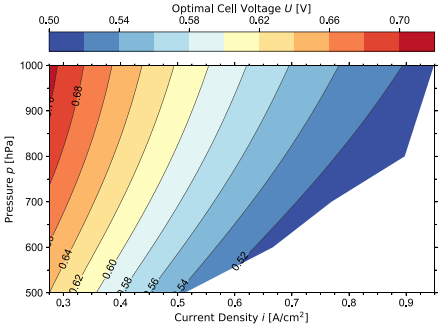

Fig. C.16. Optimized cell voltage model $U(t = 236\ \text{h}, p, i, T_{\text{opt}}, \lambda_{\text{opt}})$.

Table C.7
ANOVA of the net power model $P_{\text{net}}(t, p, i, T, \lambda)$.

Source	Sum of squares	df	Mean square	F-value	p-value
Model	2.89×10^{9}	24	1.21×10^{8}	3859.6	0
p	1.58×10^{7}	1	1.58×10^{7}	506.17	6.63×10^{-76}
i	9.47×10^{7}	1	9.47×10^{7}	3032.86	2.33×10^{-203}
T	7.41×10^{5}	1	7.41×10^{5}	23.74	1.52×10^{-06}
λ	4.71×10^{5}	1	4.71×10^{5}	15.09	0.0001
t	1.48×10^{6}	1	1.48×10^{6}	47.3	2.02×10^{-11}
pi	4.54×10^{6}	1	4.54×10^{6}	145.62	2.78×10^{-29}
pT	7.16×10^{6}	1	7.16×10^{6}	229.5	2.87×10^{-42}
$p\lambda$	1.74×10^{6}	1	1.74×10^{6}	55.91	4.32×10^{-13}
iT	1.29×10^{6}	1	1.29×10^{6}	41.18	3.50×10^{-10}
$i\lambda$	3.45×10^{5}	1	3.45×10^{5}	11.05	0.0010
$T\lambda$	2.05×10^{6}	1	2.05×10^{6}	65.81	4.67×10^{-15}
p^2	7.29×10^{6}	1	7.29×10^{6}	233.62	7.29×10^{-43}
i^2	6.23×10^{6}	1	6.23×10^{6}	199.5	7.77×10^{-38}
T^2	5.30×10^{6}	1	5.30×10^{6}	169.9	3.19×10^{-33}
λ^2	1.92×10^{6}	1	1.92×10^{6}	61.5	3.18×10^{-14}
piT	3.47×10^{6}	1	3.47×10^{6}	111.19	2.09×10^{-23}
$pi\lambda$	1.01×10^{6}	1	1.01×10^{6}	32.37	2.28×10^{-8}
$iT\lambda$	1.27×10^{6}	1	1.27×10^{6}	40.61	4.60×10^{-10}
$p^2 i$	2.43×10^{6}	1	2.43×10^{6}	77.8	2.45×10^{-17}
pi^2	1.86×10^{5}	1	1.86×10^{5}	5.95	0.0151
$i^2 T$	3.66×10^{5}	1	3.66×10^{5}	11.74	0.0007
iT^2	2.97×10^{6}	1	2.97×10^{6}	95.06	1.60×10^{-20}
$i\lambda^2$	1.25×10^{6}	1	1.25×10^{6}	40.11	5.76×10^{-10}
i^3	8.27×10^{5}	1	8.27×10^{5}	26.49	3.94×10^{-7}
Residual	1.42×10^{7}	455	31208.06		
Cor Total	2.91×10^{9}	479			

Table C.8
ANOVA of the cell voltage model $U(t, p, i, T, \lambda)$.

Source	Sum of squares	df	Mean square	F-value	p-value
Model	3.95	30	0.1316	893.03	0
p	0.0574	1	0.0574	389.39	7.20×10^{-63}
i	0.3810	1	0.3810	2585.28	2.08×10^{-188}
T	0.0109	1	0.0109	74.25	1.18×10^{-16}
λ	0.0015	1	0.0015	10.08	0.0016
t	0.0120	1	0.0120	81.24	5.79×10^{-18}
pi	0.0107	1	0.0107	72.79	2.23×10^{-16}
pT	0.0075	1	0.0075	51.04	3.68×10^{-12}
$p\lambda$	2.31×10^{-6}	1	2.31×10^{-6}	0.016	0.9004
iT	0.0043	1	0.0043	28.96	1.19×10^{-7}
$i\lambda$	0.0042	1	0.0042	28.72	1.34×10^{-7}
$T\lambda$	0.0007	1	0.0007	4.60	0.0324
p^2	0.0163	1	0.0163	110.70	2.74×10^{-23}
i^2	0.0183	1	0.0183	124.03	1.33×10^{-25}
T^2	0.0040	1	0.0040	27.43	2.51×10^{-7}
λ^2	0.0012	1	0.0012	8.17	0.0045
piT	0.0135	1	0.0135	91.57	7.26×10^{-20}
$pT\lambda$	0.0021	1	0.0021	14.06	0.0002
$iT\lambda$	0.0022	1	0.0022	15.12	0.0001
$p^2 i$	0.0172	1	0.0172	116.55	2.60×10^{-24}
$p^2 T$	0.0020	1	0.0020	13.36	0.0003
$p^2\lambda$	0.0038	1	0.0038	25.86	5.41×10^{-7}
$T^2\lambda$	0.0022	1	0.0022	14.74	0.0001
$p\lambda^2$	0.0009	1	0.0009	5.86	0.0159
$i^2\lambda$	0.0014	1	0.0014	9.46	0.0022
iT^2	0.0061	1	0.0061	41.63	2.87×10^{-10}
$i\lambda^2$	0.0017	1	0.0017	11.50	0.0008
$T^2\lambda$	0.0016	1	0.0016	10.70	0.0012
$T\lambda^2$	0.0010	1	0.0010	6.61	0.0104
T^3	0.0017	1	0.0017	11.42	0.0008
λ^3	0.0005	1	0.0005	3.10	0.0789
Residual	0.0662	449	0.00015		
Cor Total	4.0147	479			

C.2. Cell voltage model $U(t, p, i, T, \lambda)$

After dropping non-significant terms by sequential backward selection, the cell voltage model equation reads:

$$\begin{aligned} U(t,p,i,T,\lambda) = (&-5.11699 - 0.000077 \cdot t - 0.006190 \cdot p \\ &- 3.26963 \cdot i + 0.27523 \cdot T + 2.68464 \cdot \lambda \\ &- 0.001415 \cdot pi + 0.000298 \cdot pT + 0.002003 \cdot p\lambda \\ &+ 0.077289 \cdot iT + 0.842066 \cdot i\lambda - 0.085690 \cdot T\lambda \\ &- 6.19491 \times 10^{-6} \cdot p^2 - 0.155168 \cdot i^2 - 0.004878 \cdot T^2 \\ &- 0.404243 \cdot \lambda^2 + 8.93428 \times 10^{-5} \cdot piT \\ &- 4.57326 \times 10^{-5} \cdot pT\lambda - 0.009935 \cdot iT\lambda \\ &- 2.14346 \times 10^{-6} \cdot p^2 i + 6.48230 \times 10^{-8} \cdot p^2 T \\ &+ 1.01885 \times 10^{-6} \cdot p^2\lambda - 2.52677 \times 10^{-6} \cdot pT^2 \\ &- 0.000173 \cdot p\lambda^2 + 0.145297 \cdot i^2\lambda \\ &- 0.001095 \cdot iT^2 - 0.067328 \cdot i\lambda^2 + 0.000764 \cdot T^2\lambda \\ &+ 0.006496 \cdot T\lambda^2 + 0.000029 \cdot T^3 + 0.021356 \cdot \lambda^3)\ [\text{V}]\,. \end{aligned} \tag{C.2}$$

Fig. C.16 shows the contour plot of the optimized cell voltage model by applying the optimal values for stack temperature and cathode stoichiometry control, i.e. $T_{\text{opt}}(p, i)$ and $\lambda_{\text{opt}}(p, i)$, respectively. The results are shown for the center of the experimental space at $t = 236$ h. The cell voltage model's ANOVA is given in Table C.8, while the model's fit statistics is given in Table 5.

Table C.9
ANOVA of the relative humidity model $rH(p, i, T, \lambda)$.

Source	Sum of squares	df	Mean square	F-value	p-value
Model	46624.99	23	2027.17	482.23	4.10×10^{-303}
p	4518.12	1	4518.12	1074.77	5.41×10^{-122}
i	2627.59	1	2627.59	625.05	1.65×10^{-87}
T	3990.28	1	3990.28	949.21	1.64×10^{-113}
λ	1486.32	1	1486.32	353.57	8.19×10^{-59}
pi	14.06	1	14.06	3.34	0.0681
pT	0.42	1	0.42	0.10	0.7512
$p\lambda$	43.56	1	43.56	10.36	0.0014
iT	213.10	1	213.10	50.69	4.23×10^{-12}
$i\lambda$	21.91	1	21.91	5.21	0.0229
$T\lambda$	28.61	1	28.61	6.81	0.0094
p^2	114.54	1	114.54	27.25	2.73×10^{-7}
i^2	37.20	1	37.20	8.85	0.0031
T^2	7.82	1	7.82	1.86	0.1732
λ^2	82.34	1	82.34	19.59	1.20×10^{-5}
$iT\lambda$	48.20	1	48.20	11.47	0.0008
$p^2 i$	35.77	1	35.77	8.51	0.0037
pi^2	25.80	1	25.80	6.14	0.0136
$p\lambda^2$	57.36	1	57.36	13.65	0.0002
$i^2\lambda$	174.06	1	174.06	41.41	3.13×10^{-10}
$i^2 T$	134.72	1	134.72	32.05	2.67×10^{-8}
$T\lambda^2$	46.24	1	46.24	11.00	0.0010
T^3	4.65	1	4.65	1.11	0.2935
T^4	18.77	1	18.77	4.46	0.0352
Residual	1916.93	456	4.20		
Cor Total	48541.92	479			

C.3. Relative humidity model $rH(p, i, T, \lambda)$

After dropping non-significant terms by sequential backward selection, the relative humidity model equation reads:

$$\begin{aligned} rH(p,i,T,\lambda) = (&-536.11249 - 0.060655 \cdot p + 260.36793 \cdot i \\ &+ 44.21504 \cdot T + 50.50698 \cdot \lambda + 0.22378 \cdot pi \\ &- 0.000120 \cdot pT + 0.095288 \cdot p\lambda - 4.50900 \cdot iT \\ &- 88.63289 \cdot i\lambda - 2.61617 \cdot T\lambda - 3.35353 \times 10^{-6} \cdot p^2 \\ &- 251.31032 \cdot i^2 - 1.14804 \cdot T^2 - 7.10200 \cdot \lambda^2 \\ &+ 0.75385 \cdot iT\lambda - 9.36094 \times 10^{-5} \cdot p^2 i - 0.062798 \cdot pi^2 \\ &- 0.019613 \cdot p\lambda^2 + 3.08969 \cdot i^2 T + 39.54110 \cdot i^2 \lambda \\ &+ 0.46129 \cdot T\lambda^2 + 0.01377 \cdot T^3 - 0.000061 \cdot T^4) \ [\%] . \end{aligned} \tag{C.3}$$

The relative humidity model's ANOVA is given in Table C.9, while the model's fit statistics is given in Table 5.

C.4. Optimal stack temperature model $T_{opt}(p, i)$

After dropping non-significant terms by sequential backward selection, the optimal stack temperature model equation reads:

$$\begin{aligned} T_{opt}(p,i) = (&12.41121 + 0.04292 \cdot p + 87.65794 \cdot i \\ &- 0.00793 \cdot pi - 1.62157 \times 10^{-6} \cdot p^2 - 210.63948 \cdot i^2 \\ &- 1.33911 \times 10^{-6} \cdot p^2 i + 0.00799 \cdot pi^2 + 1.16779 \times 10^{-9} \cdot p^3 \\ &+ 212.65995 \cdot i^3 - 1.36030 \times 10^{-13} \cdot p^4 - 81.96024 \cdot i^4) \ [^\circ\mathrm{C}] . \end{aligned} \tag{C.4}$$

The optimal stack temperature model's ANOVA and fit statistics are given in Tables C.10 and C.11, respectively.

Table C.10
ANOVA of the optimal stack temperature model $T_{opt}(p, i)$.

Source	Sum of squares	df	Mean square	F-value	p-value
Model	1.209×10^6	11	1.099×10^5	4.807×10^7	0
p	1.696×10^5	1	1.696×10^5	7.415×10^7	0
i	5411.55	1	5411.55	2.367×10^6	0
pi	0.21	1	0.21	91.49	1.18×10^{-21}
p^2	0.07	1	0.07	28.56	9.12×10^{-8}
i^2	4.19	1	4.19	1832.01	0
$p^2 i$	0.26	1	0.26	115.19	7.76×10^{-27}
pi^2	13.73	1	13.73	6004.33	0
p^3	0.11	1	0.11	46.62	8.75×10^{-12}
i^3	130.67	1	130.67	57144.40	0
p^4	6.81×10^{-5}	1	6.81×10^{-5}	0.03	0.8630
i^4	216.48	1	216.48	94671.59	0
Residual	92.36	40389	0.0023		
Cor Total	1.209×10^6	40400			

Table C.11
Fit statistics of the optimal stack temperature model $T_{opt}(p, i)$.

RMSE	Mean	C.V. %	R^2	Adj. R^2	Pred. R^2	Adeq. Prec.
0.0478	54.53	0.0877	0.9999	0.9999	0.9999	25021.53

Table C.12
ANOVA of the optimal cathode stoichiometry model $\lambda_{opt}(p, i)$.

Source	Sum of squares	df	Mean square	F-value	p-value
Model	776.64	11	70.60	6.297×10^5	0
p	66.68	1	66.68	5.947×10^5	0
i	31.02	1	31.02	2.767×10^5	0
pi	0.38	1	0.38	3462.28	0
p^2	0.0311	1	0.0311	277.12	5.13×10^{-62}
i^2	0.1137	1	0.1137	1014.03	8.49×10^{-220}
$p^2 i$	0.1149	1	0.1149	1024.91	4.18×10^{-222}
pi^2	5.03	1	5.03	44872.29	0
p^3	0.0004	1	0.0004	3.60	0.0578
i^3	0.7693	1	0.7693	6860.84	0
p^4	0.0010	1	0.0010	8.84	0.0029
i^4	5.88	1	5.88	52415.31	0
Residual	4.53	40389	0.00011		
Cor Total	781.17	40400			

Table C.13
Fit statistics of the optimal cathode stoichiometry model $\lambda_{opt}(p, i)$.

RMSE	Mean	C.V. %	R^2	Adj. R^2	Pred. R^2	Adeq. Prec.
0.0106	2.81	0.3773	0.9942	0.9942	0.9942	4287.4774

C.5. Optimal cathode stoichiometry model $\lambda_{opt}(p, i)$

After dropping non-significant terms by sequential backward selection, the optimal cathode stoichiometry model equation reads:

$$\begin{aligned} \lambda_{opt}(p,i) = &\ 6.19857 - 0.00129 \cdot p - 16.58180 \cdot i \\ &+ 0.00491 \cdot pi - 2.21063 \times 10^{-6} \cdot p^2 + 34.94368 \cdot i^2 \\ &+ 8.84484 \times 10^{-7} \cdot p^2 i - 0.00484 \cdot pi^2 + 1.60395 \times 10^{-9} \cdot p^3 \\ &- 33.70819 \cdot i^3 - 5.19071 \times 10^{-13} \cdot p^4 + 13.50416 \cdot i^4 . \end{aligned} \tag{C.5}$$

The optimal cathode stoichiometry model's ANOVA and fit statistics are given in Tables C.12 and C.13, respectively.

Appendix D. Supplementary data

Supplementary material related to this article can be found online at https://doi.org/10.1016/j.enconman.2025.120251.

Data availability

Data will be made available on request.

References

[1] Pratt JW, Klebanoff LE, Munoz-Ramos K, Akhil AA, Curgus DB, Schenkman BL. Proton exchange membrane fuel cells for electrical power generation on-board commercial airplanes. Appl Energy 2013;101:776–96. http://dx.doi.org/10.1016/j.apenergy.2012.08.003.

[2] Guida D, Minutillo M. Design methodology for a PEM fuel cell power system in a more electrical aircraft. Appl Energy 2017;192:446–56. http://dx.doi.org/10.1016/j.apenergy.2016.10.090.

[3] Kadyk T, Winnefeld C, Hanke-Rauschenbach R, Krewer U. Analysis and design of fuel cell systems for aviation. Energies 2018;11(2):375. http://dx.doi.org/10.3390/en11020375.

[4] Kazula S, De Graaf S, Enghardt L. Review of fuel cell technologies and evaluation of their potential and challenges for electrified propulsion systems in commercial aviation. J Glob Power Propuls Soc 2023;7:43–57. http://dx.doi.org/10.33737/jgpps/158036.

[5] Massaro MC, Pramotton S, Marocco P, Monteverde AHA, Santarelli M. Optimal design of a hydrogen-powered fuel cell system for aircraft applications. Energy Convers Manage 2024;306:118266. http://dx.doi.org/10.1016/j.enconman.2024.118266.

[6] Song WJ, Chen H, Guo H, Ye F, Li JR. Research progress of proton exchange membrane fuel cells utilizing in high altitude environments. Int J Hydrog Energy 2022;47(59):24945–62. http://dx.doi.org/10.1016/j.ijhydene.2022.05.238.

[7] Barbir F. PEM fuel cells: theory and practice. 2nd ed. Amsterdam; Boston: Academic Press; 2013.

[8] Werner C, Busemeyer L, Kallo J. The impact of operating parameters and system architecture on the water management of a multifunctional PEMFC system. Int J Hydrog Energy 2015;40(35):11595–603. http://dx.doi.org/10.1016/j.ijhydene.2015.02.012.

[9] Schröter J, Graf T, Frank D, Bauer C, Kallo J, Willich C. Influence of pressure losses on compressor performance in a pressurized fuel cell air supply system for airplane applications. Int J Hydrog Energy 2021;46(40):21151–9. http://dx.doi.org/10.1016/j.ijhydene.2021.03.218.

[10] Pratt JW, Brouwer J, Samuelsen GS. Performance of proton exchange membrane fuel cell at high-altitude conditions. J Propuls Power 2007;23(2):437–44. http://dx.doi.org/10.2514/1.20535.

[11] Haraldsson K, Alvfors P. Effects of ambient conditions on fuel cell vehicle performance. J Power Sources 2005;145(2):298–306. http://dx.doi.org/10.1016/j.jpowsour.2004.12.080.

[12] Renouard-Vallet G, Saballus M, Schmithals G, Schirmer J, Kallo J, Friedrich KA. Improving the environmental impact of civil aircraft by fuel cell technology: Concepts and technological progress. Energy Environ Sci 2010;3(10):1458–68. http://dx.doi.org/10.1039/b925930a.

[13] Willich C, Frank D, Graf T, Wazlawik S, Brandao S, Bauer C. High-altitude operation of a commercial 100 kW PEM fuel cell system. Energies 2024;17(24):6309. http://dx.doi.org/10.3390/en17246309.

[14] Schröder M, Becker F, Gentner C. Optimal design of proton exchange membrane fuel cell systems for regional aircraft. Energy Convers Manage 2024;308:118338. http://dx.doi.org/10.1016/j.enconman.2024.118338.

[15] Chang V, Gallman J. Altitude testing of fuel cell systems for aircraft applications. In: SAE transactions, vol. 113, SAE International; 2004, p. 1943–57, arXiv:44738079.

[16] Spiegel R, Gilchrist T, House D. Fuel cell bus operation at high altitude. Proc Inst Mech Eng Part A: J Power Energy 1999;213(1):57–68. http://dx.doi.org/10.1243/0957650991537437.

[17] Graf T, Fonk R, Paessler S, Bauer C, Kallo J, Willich C. Low pressure influence on a direct fuel cell battery hybrid system for aviation. Int J Hydrog Energy 2024;50:672–81. http://dx.doi.org/10.1016/j.ijhydene.2023.09.003.

[18] International Civil Aviation Organization (ICAO). Manual of the ICAO standard atmosphere, extended to 80 kilometres (262 500 feet). 1993.

[19] Hordé T, Achard P, Metkemeijer R. PEMFC application for aviation: Experimental and numerical study of sensitivity to altitude. Int J Hydrog Energy 2012;37(14):10818–29. http://dx.doi.org/10.1016/j.ijhydene.2012.04.085.

[20] Werner C, Gores F, Busemeyer L, Kallo J, Heitmann S, Griebenow M. Characteristics of PEMFC operation in ambient- and low-pressure environment considering the fuel cell humidification. CEAS Aeronaut J 2015;6(2):229–43. http://dx.doi.org/10.1007/s13272-014-0142-z.

[21] Werner C, Preiß G, Gores F, Griebenow M, Heitmann S. A comparison of low-pressure and supercharged operation of polymer electrolyte membrane fuel cell systems for aircraft applications. Prog Aerosp Sci 2016;85:51–64. http://dx.doi.org/10.1016/j.paerosci.2016.07.005.

[22] Pessot A, Turpin C, Jaafar A, Soyez E, Rallières O, Gager G, et al. Contribution to the modelling of a low temperature PEM fuel cell in aeronautical conditions by design of experiments. Math Comput Simulation 2019;158:179–98. http://dx.doi.org/10.1016/j.matcom.2018.07.008.

[23] Chen J, He H, Yue H. A review of plateau environmental adaptation for proton exchange membrane fuel cells. Int J Hydrog Energy 2024;50:744–64. http://dx.doi.org/10.1016/j.ijhydene.2023.09.014.

[24] Li Y, Hu Z, Liu H, Xu L, Li J, Xu L, et al. Comprehensive analysis of cathode air pressure of fuel cell powertrain system of aircraft: Performance, efficiency, and control. Energy Convers Manage 2023;283:116903. http://dx.doi.org/10.1016/j.enconman.2023.116903.

[25] Li S, Qiu Y, Yin L, Li R, Gan R, Li Q, et al. Net power optimization based on extremum search and model-free adaptive control of PEMFC power generation system for high altitude. IEEE Trans Transp Electrification 2023;9(4):5151–64. http://dx.doi.org/10.1109/TTE.2022.3222970.

[26] Xie S, Li Q, Yin L, Huo S, Wang T, Chen W. Multivariable cooperative control for performance guarantee of PEMFC system in high-altitude environment. IEEE Trans Ind Electron 2024;71(12):15846–57. http://dx.doi.org/10.1109/TIE.2024.3390742.

[27] Jiang F, Wei Z, Zhang C, He H, Song R, Gao F. Cathodic supply optimization of PEMFC system under variable altitude. IEEE Trans Ind Electron 2024;71(11):14298–307. http://dx.doi.org/10.1109/TIE.2024.3368097.

[28] Chen J, He H, Quan S, Wei Z, Zhang Z, Wang Y-X. Real-time power optimization based on PSO feedforward and perturbation & observation of fuel cell system for high altitude. Fuel 2024;356:129551. http://dx.doi.org/10.1016/j.fuel.2023.129551.

[29] Hydrogenics Corporation. HyPM HD 10-120 Product Manual, Mississauga, Ontario, Canada. 2018.

[30] Jabbary A, Rostami Arnesa S, Samanipour H, Ahmadi N. Numerical investigation of 3D rhombus designed PEMFC on the cell performance. Int J Green Energy 2021;18(5):425–42. http://dx.doi.org/10.1080/15435075.2020.1865361.

[31] Jabbary A, Pourmahmoud N, Abdollahi MAA, Rosen MA. Artificial intelligence-assisted optimization and multiphase analysis of polygon PEM fuel cells. Int J Green Energy 2024;21(7):1550–66. http://dx.doi.org/10.1080/15435075.2023.2262006.

[32] Pei H, Xiao C, Tu Z. Experimental study on liquid water formation characteristics in a novel transparent proton exchange membrane fuel cell. Appl Energy 2022;321:119349. http://dx.doi.org/10.1016/j.apenergy.2022.119349.

[33] Taylor JR. An introduction to error analysis: the study of uncertainties in physical measurements. 2nd ed. Sousalito, California: University Science Books; 1997.

[34] Montgomery DC. Design and analysis of experiments, 8th ed. Hoboken, NJ: John Wiley & Sons, Inc; 2013.

[35] Dean A, Voss D, Draguljić D. Design and analysis of experiments, 2nd ed. Springer texts in statistics, Cham: Springer International Publishing; 2017, http://dx.doi.org/10.1007/978-3-319-52250-0.

[36] Meiler M, Andre D, Pérez Á, Schmid O, Hofer E. Nonlinear D-optimal design of experiments for polymer–electrolyte–membrane fuel cells. J Power Sources 2009;190(1):48–55. http://dx.doi.org/10.1016/j.jpowsour.2008.08.068.

[37] Kanani H, Shams M, Hasheminasab M, Bozorgnezhad A. Model development and optimization of operating conditions to maximize PEMFC performance by response surface methodology. Energy Convers Manage 2015;93:9–22. http://dx.doi.org/10.1016/j.enconman.2014.12.093.

[38] Labach I, Rallières O, Turpin C. Steady-state semi-empirical model of a single proton exchange membrane fuel cell (PEMFC) at varying operating conditions. Fuel Cells 2017;17(2):166–77. http://dx.doi.org/10.1002/fuce.201600074.

[39] Silva V, Eusébio D, Cardoso J, Zhiani M, Majidi S. Targeting optimized and robust operating conditions in a hydrogen-fed proton exchange membrane fuel cell. Energy Convers Manage 2017;154:149–56. http://dx.doi.org/10.1016/j.enconman.2017.10.053.

[40] Boyaci San FG, Dursun S, Yazici MS. Optimization of the PEMFC operating parameters for cathode in the presence of PtCo/CVD graphene using factorial design. Int J Energy Res 2019;43(9):4506–19. http://dx.doi.org/10.1002/er.4579.

[41] Kahveci EE, Taymaz I. Hydrogen PEMFC stack performance analysis through experimental study of operating parameters by using response surface methodology (RSM). Int J Hydrog Energy 2022;47(24):12293–303. http://dx.doi.org/10.1016/j.ijhydene.2021.09.119.

[42] Wahdame B, Candusso D, Francois X, Harel F, Kauffmann J, Coquery G. Design of experiment techniques for fuel cell characterisation and development. Int J Hydrog Energy 2009;34(2):967–80. http://dx.doi.org/10.1016/j.ijhydene.2008.10.066.

[43] Karanfil G. Importance and applications of DOE/Optimization methods in PEM fuel cells: A review. Int J Energy Res 2020;44(1):4–25. http://dx.doi.org/10.1002/er.4815.

[44] The MathWorks Inc. Statistics and machine learning toolbox version: 9.11 (R2021b). Natick, Massachusetts, United States: The MathWorks Inc.; 2021.

[45] Dicks A, Rand DAJ. Fuel cell systems explained. 3rd ed. Hoboken, NJ, USA: Wiley; 2018.

[46] Stat-Ease Inc. Stat-Ease 360 version: 23. Minneapolis, MN, USA: Stat-Ease Inc.; 2023.

[47] Kleppmann W. Versuchsplanung - Produkte und Prozesse optimieren. 10th ed. München: Carl Hanser Verlag; 2020.

[48] Siebertz K, Van Bebber D, Hochkirchen T. Statistische Versuchsplanung. 2nd ed. Berlin, Heidelberg: Springer Berlin Heidelberg; 2017, http://dx.doi.org/10.1007/978-3-662-55743-3.

[49] Settele J. Experimental investigation of a PEMFC system operated under low pressure conditions. Stuttgart, Germany: University of Stuttgart; 2023.
[50] Alduchov OA, Eskridge RE. Improved magnus form approximation of saturation vapor pressure. Am Meteorol Soc 1996;35:601–9. http://dx.doi.org/10.1175/1520-0450(1996)035<0601:IMFAOS>2.0.CO;2.
[51] Gazdzick P, Mitzel J, Garcia Sanchez D, Schulze M, Friedrich KA. Evaluation of reversible and irreversible degradation rates of polymer electrolyte membrane fuel cells tested in automotive conditions. J Power Sources 2016;327:86–95. http://dx.doi.org/10.1016/j.jpowsour.2016.07.049.
[52] Mitzel J, Zhang Q, Gazdzicki P, Friedrich KA. Review on mechanisms and recovery procedures for reversible performance losses in polymer electrolyte membrane fuel cells. J Power Sources 2021;488:229375. http://dx.doi.org/10.1016/j.jpowsour.2020.229375.
[53] IAPWS. Industrial formulation 1997 for the thermodynamic properties of water and steam. Tech. rep. IAPWS R7-97, Lucerne, Swizerland: The International Association for the Properties of Water and Steam; 2007, p. 49.